Cell Reports

Resource

Proteomics analysis of adipose depots after intermittent fasting reveals visceral fat preservation mechanisms

Graphical Abstract

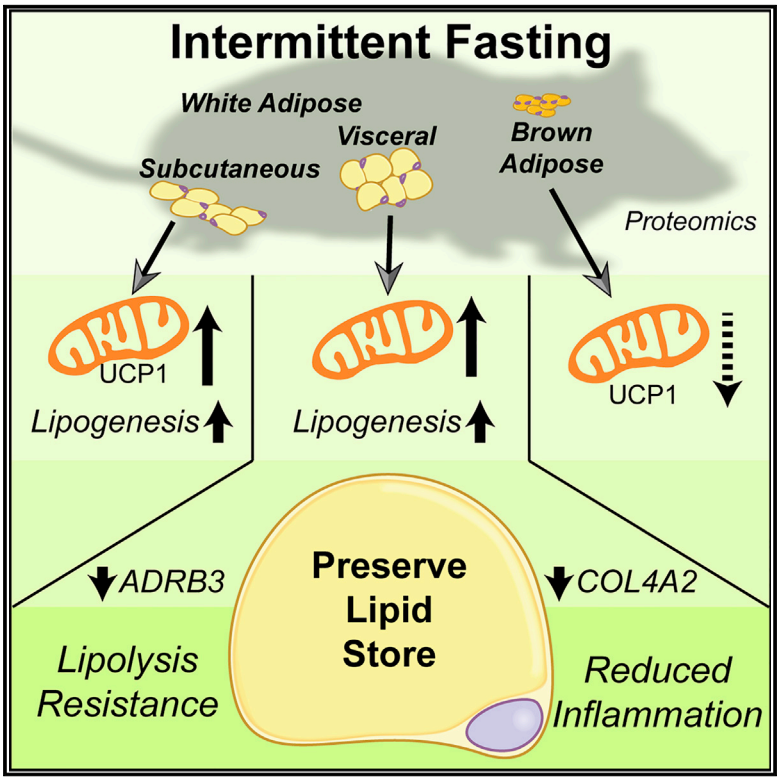

Highlights

- Every-other-day fasting (EODF) has depot-specific effects on the adipose proteome
- EODF leads to suppression of lipolysis in vWAT by repression of ADRB3
- Mitochondrial content and fatty acid synthesis enzymes are higher in WAT after EODF
- EODF reduces inflammatory extracellular matrix components of vWAT

Authors

Dylan J. Harney, Michelle Cielesh, Renee Chu, Kristen C. Cooke, David E. James, Jacqueline Stöckli, Mark Larance

Correspondence

mark.larance@sydney.edu.au

In brief

Harney et al. show that every-other-day fasting improves metabolic health in mice in the absence of weight loss and examine the proteomic response of several key adipose depots. They find depot-specific increases in mitochondria, suppression of lipolysis, increased fatty acid synthesis, and changes in extracellular matrix content.

Harney et al., 2021, Cell Reports *34*, 108804
March 2, 2021
https://doi.org/10.1016/j.celrep.2021.108804

CellPress

Cell Reports

CellPress
OPEN ACCESS

Resource

Proteomics analysis of adipose depots after intermittent fasting reveals visceral fat preservation mechanisms

Dylan J. Harney,[1] Michelle Cielesh,[1] Renee Chu,[1] Kristen C. Cooke,[1] David E. James,[1,2] Jacqueline Stöckli,[1] and Mark Larance[1,3,*]

[1]Charles Perkins Centre, School of Life and Environmental Sciences, University of Sydney, Camperdown, NSW, Australia
[2]School of Medical Sciences, University of Sydney, Camperdown, NSW, Australia
[3]Lead contact
*Correspondence: mark.larance@sydney.edu.au
https://doi.org/10.1016/j.celrep.2021.108804

SUMMARY

Intermittent fasting is a beneficial dietary treatment for obesity. But the response of each distinct adipose depot is currently poorly defined. Here we explore the response of key adipose depots to every-other-day fasting (EODF) in mice using proteomics. A key change in subcutaneous white adipose tissue (scWAT) and visceral WAT (vWAT) depots is an increase in mitochondrial protein content after EODF. This effect is correlated with increased fatty acid synthesis enzymes in both WAT depots but not in brown adipose tissue. Strikingly, EODF treatment downregulates lipolysis specifically in vWAT, mediated by a large decrease in the abundance of the catecholamine receptor (ADRB3). Together, these changes are important for preservation of the visceral lipid store during EODF. Enrichment analysis highlights downregulation of inflammatory collagen IV specifically in vWAT, allowing improved insulin sensitivity. This resource for adipose-depot-specific fasting adaptations in mice is available using a web-based interactive visualization.

INTRODUCTION

Obesity is a risk factor for numerous cancers, heart disease, and type 2 diabetes (Hayes et al., 2017; Kopelman, 2000). To counteract metabolic dysfunction, numerous dietary interventions have been trialed; one of the most popular is intermittent fasting (IF) (Seimon et al., 2015). In humans and rodents, IF has been demonstrated to lower fasted insulin levels, improve glucose tolerance, and lower blood cholesterol (Anson et al., 2003; Goodrick et al., 1990; Li et al., 2017; Xie et al., 2017), even in the absence of weight loss (Patterson and Sears, 2017; Varady and Gabel, 2019; Wilkinson et al., 2020). IF strategies can be roughly split into two categories; time-restricted feeding (TRF), where food is only consumed during a restricted time window each day, or every-other-day fasting (EODF), where there are alternating days of fasting and feeding (Chaix et al., 2014; Heilbronn et al., 2005; Li et al., 2017; Liu et al., 2019; Varady et al., 2010; Xie et al., 2017). EODF is a simpler and more easily implemented strategy and has been established to be more tolerable in human trials (Barnosky et al., 2014). This makes EODF an attractive option for combating metabolic disease, but the molecular mechanisms underlying the beneficial effects are not completely understood.

Adipose tissue plays a central role in regulating the acute fasting response. With a lowered blood glucose level during fasting, circulating insulin abundance is low, and glucagon abundance is high (Habegger et al., 2010), which acts to maintain blood glucose levels primarily through actions in the liver. These stimuli, alongside release of other hormones such as leptin, lead to release of catecholamines via the sympathetic nervous system (Lafontan and Langin, 2009; Pan and Myers, 2018; Zechner et al., 2017). Sympathetic neurons can secrete norepinephrine locally or trigger the adrenal gland to release epinephrine systemically (Wang et al., 2016). These molecules induce lipolysis through adrenergic receptor signaling, which triggers release of non-esterified fatty acids (NEFAs) from white adipose tissue (WAT) (Zechner et al., 2017), providing fuel for other tissues during fasting. Concomitant to providing these NEFAs as fuel, WAT releases numerous hormones, such as adiponectin (Scheja and Heeren, 2019), which acts to improve tissue uptake of glucose and NEFAs.

Adding to this complex role, different adipose depots exhibit distinct phenotypes in response to fasting. In general, adipose depots can be split into WAT and brown adipose tissue (BAT) based on its color and developmental origin. WAT itself can be further divided into visceral WAT (vWAT) and subcutaneous WAT (scWAT) based on localization in or outside of the abdominal cavity, respectively. In humans and rodents, high amounts of vWAT have been correlated positively with insulin resistance, cardiovascular disease, cancer, and high morbidity (Després, 2012; Després and Lemieux, 2006; Renehan et al., 2008). vWAT is the depot most sensitive to lipolysis (Arner, 2005; Wajchenberg, 2000; Zechner et al., 2017). In contrast, scWAT is the largest adipose depot in humans and mice, where increased scWAT is associated with lower metabolic disease risk (Fox

et al., 2007; Kwon et al., 2017; Liu et al., 2010; Vitali et al., 2012). scWAT is also more highly innervated and vascularized, with higher resistance to adrenergic stimulation of lipolysis (Farb and Gokce, 2015; Guilherme et al., 2019). BAT is the smallest fat depot, located around the neck and interscapular space, and has the fundamentally different role of providing heat through non-shivering thermogenesis (Kajimura et al., 2010, 2015). At a cellular level, these differences are manifested by BAT having a greater accumulation of mitochondria and smaller, multi-locular fat droplets (Bartelt and Heeren, 2014). These depots are not completely distinct, however, because scWAT displays some similarities to BAT under specific physiological conditions (Ohno et al., 2012). For example, scWAT undergoes "browning," where adipocytes accumulate mitochondria, the lipid droplet becomes multi-locular, and there is increased expression of BAT-specific proteins, such as uncoupling protein 1 (*UCP1*), in response to stressors, including prolonged cold exposure (Bartelt and Heeren, 2014; Ohno et al., 2012; Vitali et al., 2012).

Recently, IF has been demonstrated to induce changes in adipose tissue (Kim et al., 2017, 2019; Li et al., 2017). Studies examining scWAT in mice have confirmed a browning response to IF, with increased abundance of the *UCP1* protein and increased body temperature (Kim et al., 2017, 2019; Li et al., 2017). Conversely, the mitochondrial content in the BAT of IF diet mice has been shown to be decreased, with the abundance of *UCP1* mRNA and protein decreased after IF (Desautels and Dulos, 1988; Li et al., 2017). However, the effect of this change in BAT is unclear. These studies show the importance of browning of scWAT in the response to IF, but no study has provided a comprehensive analysis of the IF-induced changes in all three adipose depots (vWAT, scWAT, and BAT).

In this study, we performed an unbiased proteomic analysis to identify changes in protein abundance that were altered significantly in any of the three different adipose depots, using the previously established IF model of EODF (Harney et al., 2019a; Hatchwell et al., 2020; Kim et al., 2017, 2019; Li et al., 2017). This analysis examined the differences between the acute fasting response and the response to EODF in each adipose depot. We showed that EODF increased the mitochondrial protein content of vWAT and scWAT to similar extents but, as shown previously, only induced UCP1 protein expression in scWAT. Surprisingly, we observed that the lipolysis pathway of the vWAT depot was reduced dramatically by EODF, whereas fatty acid synthesis pathways in vWAT and scWAT were increased greatly by EODF treatment. These data show the significant and unique changes vWAT has undergone to preserve the lipid store during the repeated fasting bouts of the IF diet regimen. This global data resource for adipose depot fasting responses is provided as a free web-based visualization for the research community (https://www.larancelab.com/fat-eodf).

RESULTS

The EODF model improves metabolic health and glucose tolerance

To examine the effects of IF on the adipose tissue proteome, an EODF model was applied for 2 weeks to adult (8-week-old) male C57BL/6J mice compared with an equal number of control mice fed *ad libitum* (AL), as established previously (Hatchwell et al., 2020; Kim et al., 2017, 2019; Li et al., 2017; Xie et al., 2017). Animals on the EODF diet showed a minor but non-significant decrease in total food intake and no change in body weight when measured on feeding days (Figures S1A and S1B). If the duration of EODF treatment is extended to match other studies (4–16 weeks), the small decrease in total food intake may result in a total body weight decrease, as seen previously (Kim et al., 2017; Li et al., 2017; Liu et al., 2019; Xie et al., 2017), which could have additional effects on the proteome that we aimed to avoid. As expected, EODF mice displayed a significantly lower area under the curve (AUC) compared with the group fed *ad libitum*, with similar fat and lean masses (Figures S1C and S1D). The small decrease in lean mass we observed is most likely due to consumption of muscle mass for substrates that may be used by the liver to fuel gluconeogenesis (Hui et al., 2020). Of the AL and EODF mice, half were sacrificed after 16 h of *ad libitum* access to food (fed harvest) or after 16 h of no food access (fasted harvest); n = 5 per condition. Tissues were harvested and flash frozen in liquid nitrogen. This study focuses on three key adipose depots: vWAT derived from the gonadal fat pad, inguinal scWAT, and interscapular BAT. For protein extraction from the adipose depots, a workflow incorporating chloroform-methanol precipitation was used to remove the large amounts of lipids that would otherwise confound the protein analysis (Figure 1A).

EODF-induced, adipose-depot-specific proteome responses

Mass spectrometry-based proteomics allows unbiased analysis of protein abundance in a lysate, enabling monitoring of various metabolic and signaling pathways across the multiple adipose depots in each animal. Each adipose tissue sample was lysed, trypsin digested, and analyzed by liquid chromatography-tandem mass spectrometry (LC-MS/MS). These data were processed in MaxQuant (Cox and Mann, 2008) using label-free quantification (LFQ) (Figure 1A). From this analysis, more than 8,500 proteins were identified across the depots (Table S1) from more than 125,000 peptides (Table S2). To determine the proteins in each depot that were affected significantly by EODF or acute fasting, a two-way ANOVA was performed on each protein that was detected in at least 3 mice per condition and tissue. Subsequent p values were adjusted for multiple hypothesis testing using Benjamini-Hochberg correction. From this analysis, ~1,800 proteins were changing significantly in at least 1 depot in response to EODF irrespective of harvest state. Conversely, only ~130 proteins were changing significantly in at least 1 depot in response to acute fasting irrespective of the EODF intervention. This large difference in proteome response between EODF and acute fasting suggests that the changes with EODF are likely amplified by the repeated fasting bouts. To visualize these changes, a heatmap was generated for proteins detected in all depots that were affected significantly by EODF in at least one depot (Figure 1B). Comparing the trends in protein abundance across tissues, vWAT and scWAT appeared to follow the same general response to EODF but with scWAT generally having a lower fold change than vWAT. In contrast, BAT showed comparatively minor responses to

CellPress
OPEN ACCESS

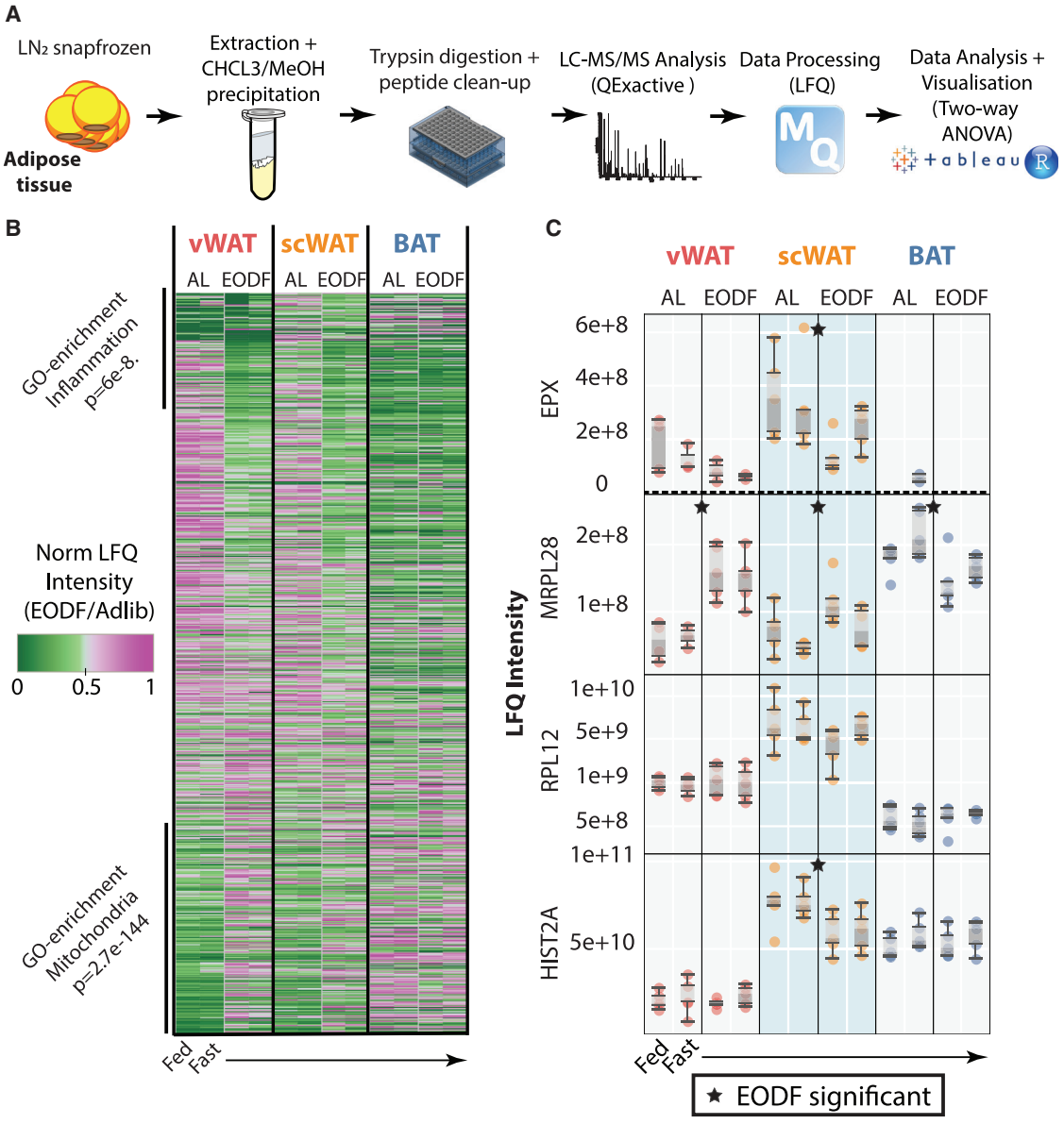

(legend on next page)

EODF. This comparison also indicated that vWAT and scWAT were becoming more like BAT after EODF. To identify the pathways dominating this change after EODF in vWAT and scWAT, enrichment analysis was employed on the heatmap proteins and showed that ~50% of the 500 most upregulated proteins were mitochondrial (GO cellular compartment, p = 1.79e−140). The most downregulated proteins after EODF demonstrated enrichment in the innate immune response (reactome, p < 9.6e−9), similar to previous studies of human plasma after IF (Harney et al., 2019a, 2019b). To examine these changes in more detail, several boxplots were generated (Figure 1C) including two controls, the large ribosomal subunit protein 12 (*RPL12*) and core histone H2A (*HIST2A*), which did not show a significant change for any depot in response to EODF or acute fasting. An interesting example of an EODF-regulated innate immune response protein was eosinophil peroxidase (*EPX*), which was decreased in both WAT depots in response to EODF. Similarly, many macrophage-specific proteins, such as CD14 and CD163 (Figure S2), were also decreased in both WAT depots but not in BAT. In contrast, the mitochondrial ribosomal protein *MRPL28* was increased significantly in both WAT depots after EODF. To comprehensively visualize the mitochondrial protein response to EODF, volcano plots of all proteins detected in each depot were generated, with colored circles representing mitochondrion-derived proteins (Figure 1D). These plots showed that, in vWAT and scWAT, mitochondrial protein abundance was increased by approximately 2-fold in response to EODF. In contrast, mitochondrial proteins were decreased by 2-fold in BAT after EODF, in agreement with previous studies (Desautels and Dulos, 1988; Li et al., 2017).

EODF and acute fasting induced unique changes in adipose proteomes

To further dissect the differences between the EODF response and the acute fasting response in each adipose depot, scatterplots were generated for proteins changed significantly (false discovery rate [FDR] < 5%, fold change > 2) in the diet variable (EODF/adlib) (Figures 2A, 2C, and 2E) or the harvest state variable (acute fasted/fed) (Figures 2B, 2D, and 2F). The fold change in response to diet or harvest state is shown on the axes. Across all depots, the number of acute fasting-regulated proteins was much less than EODF-regulated proteins. Most proteins regulated by acute fasting were distinct from those altered by EODF. Pathway analysis was conducted on the proteins from these plots using gene set enrichment analysis (GSEA) (Subramanian et al., 2005). In vWAT, the most upregulated gene set after EODF was peroxisomal proliferation activation receptor gamma coactivator 1 alpha (*PGC1alpha*) target genes (Table S3). PGC1alpha targets, including estrogen related-receptor alpha (*ESRRalpha*), induce mitogenesis and increase lipid oxidation (Arany et al., 2008; Huss et al., 2002; Mootha et al., 2004; Schreiber et al., 2004). Similarly enriched were mitochondrial gene sets related to pyruvate metabolism, fatty acid metabolism, and the TCA cycle. EODF upregulated many of the same gene sets in scWAT as in vWAT, including *ESRRalpha* targets for mitogenesis and fatty acid synthesis pathways. Conversely, in BAT there was consistent enrichment of mitochondrial gene sets in proteins that were downregulated by EODF, which again supports a decrease in mitochondrial protein content in BAT after EODF.

The most downregulated gene sets by EODF in vWAT included those related to the extracellular matrix (ECM), which was interesting given that IF has not been shown previously to affect adipose ECM composition. This included a significant reduction in several collagen proteins, including IV and VI (Figure 4A; Table S3). However, unlike in vWAT, there was no decrease in ECM-related gene sets in scWAT after EODF. To visualize these changes in the ECM, vWAT and scWAT were fixed in formalin and stained with H&E and picrosirius red, which stains for collagen and other ECM proteins. H&E staining demonstrated a reduction in adipocyte size in vWAT and scWAT, consistent with previous studies (Figure 4B), but there was no observable change in staining with picrosirius red in either tissue (Figure S3). This suggests that the total level of all collagens as detected by the stain is unaltered by EODF.

EODF increased fatty acid synthesis in WAT but not BAT

Concomitant with these analyses, we examined proteins with the largest significant fold changes in response to EODF in the vWAT depot. The most upregulated proteins in EODF were fatty acid synthesis enzymes, including ATP-citrate lyase (*ACLY*) and the acetyl-coenzyme A (CoA) carboxylase interactor thyroid hormone-inducible hepatic protein (*THRSP*) (Figures 2A and 3A). The proteins most downregulated by EODF in vWAT included the *PPARgamma* target gamma-synuclein (*SNCG*) (Dunn et al., 2015) and the plasma contaminant proteins haptoglobin (*HP*) and alpha1-antitrypsin (*SERPINA1E*). In acutely fasted vWAT, phosphoenolpyruvate carboxykinase 1 (*PCK1*) was the only significantly upregulated protein, whereas the cholesterol synthesis enzyme 3-hydroxy-3-methylglutaryl-CoA-Synthase 1 (*HMGCS1*) was one of the most downregulated (Figures 2B and 3C). Pantothenate kinase 3 (*PANK3*) (Figure 3A) showed the largest interaction between EODF and acute fasting, where the 8-fold upregulation with EODF in the fed state was abolished in the fasted state.

Figure 1. Proteomics analysis of adipose tissue response to EODF reveals differential regulation of mitogenesis

(A) Workflow of adipose tissue processing for mass spectrometry.

(B) Heatmap of adipose tissue proteomics, analyzed using 2-way ANOVA, where green represents low protein abundance and pink represents high protein abundance. Only proteins that were changed significantly by EODF in at least one depot are displayed. Each column represents the average of 5 mice, where the LFQ intensity has been normalized. Data are sorted by EODF fold change in vWAT.

(C) Box-and-whisker plots for specific proteins of interest. Each point represents the protein abundance for an individual mouse. Black stars represent diet significance and black squares represent harvest state significance ($p < 0.05$) in that tissue. Error bars represent 1.5 times the interquartile range.

(D) Volcano plot of the $\log_2$ fold change of EODF over *ad libitum* protein abundance for mice in the fed state (n = 5 per condition) on the x axis and $\log_{10}$ of the p value derived from a 2-way ANOVA for EODF effect corrected for multiple hypothesis testing with Benjamini-Hochberg correction. Each point represents an individual protein; colored circles represent a mitochondrial protein, and gray circles represent non-mitochondrial proteins. The dashed line represents the significance threshold.

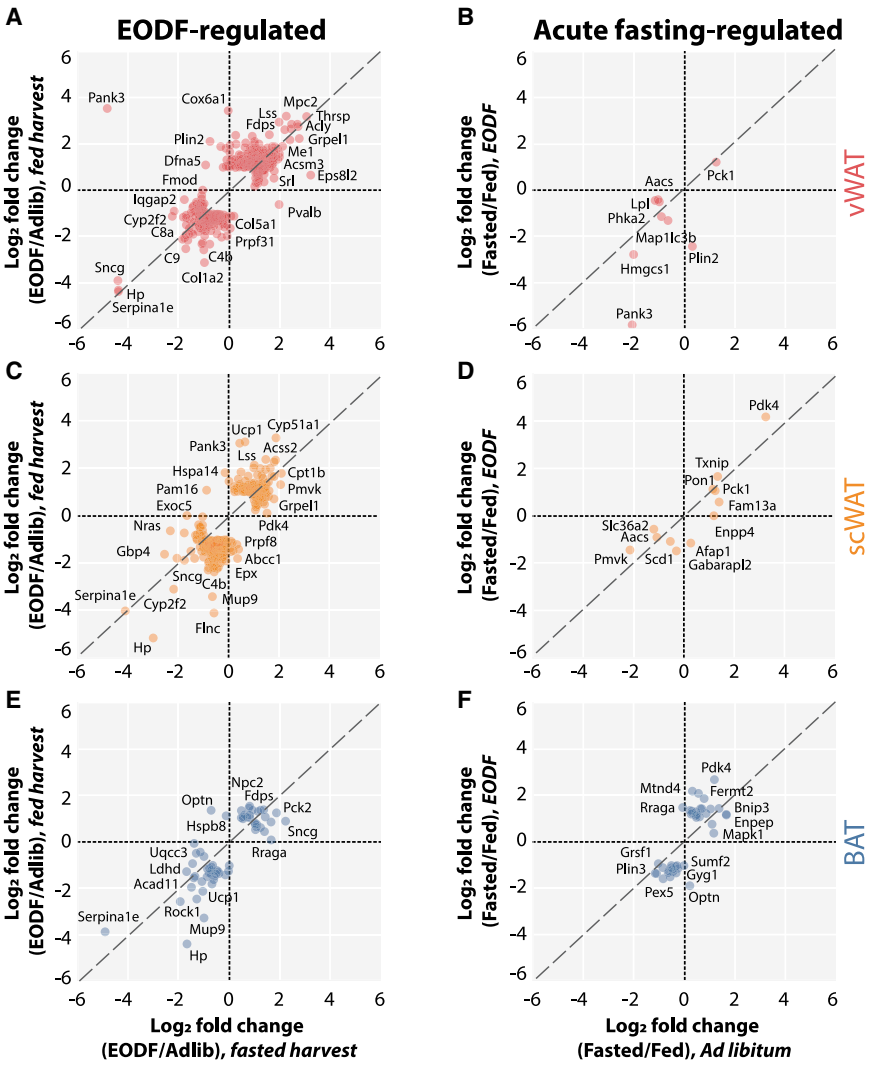

Figure 2. Proteomics analysis reveals unique adipose-depot-specific responses to EODF and acute fasting

(A, C, and E) Proteins that were regulated significantly ($p < 0.05$) by EODF were plotted as points with Log_2 fold change (>2) for EODF/*ad libitum* response, shown on the y axis for overnight-fed animals and on the x axis for overnight-fasted animals. n = 5 animals per condition.

(B, D, and F) Proteins that were regulated significantly ($p < 0.05$) by acute fasting were plotted as points with Log_2 fold change (>2) for the overnight fasting/overnight feeding response, shown on the y axis for EODF animals and on the x axis for animals fed *ad libitum*. n = 5 per animals per condition.

As in vWAT, fatty acid synthesis enzymes were among the most upregulated in scWAT after EODF, including acyl-coenzyme synthase 2 (*ACSS2*); however, in this depot, we observed the strongest downregulation of several innate immunity proteins, such as complement 4b (*C4b*) (Figure 3A) and eosinophil peroxidase (*EPX*) (Figure 2C). Proteins involved in nutrient uptake and catabolism, including pyruvate dehydrogenase kinase 4 (*PDK4*) and thioredoxin-interacting protein (*TXNIP*) (Figure 3B), were increased the most by acute fasting in scWAT (Figure 2D). The cholesterol synthesis enzyme phosphomevalonate kinase (*PMVK*) and stearoyl-CoA desaturase 1 (*SCD1*) (Figure 3A) were the most downregulated proteins in scWAT after acute fasting. The changes in *PANK3* and *SNCG* observed in vWAT were replicated in scWAT but with smaller fold changes (Figures 2C and 3A). Interestingly, uncoupling protein 1 (*UCP1*), which is associated with adipose browning, was increased by EODF only in scWAT, as shown previously (Kim et al., 2017, 2019; Li et al., 2017).

The BAT response to EODF and acute fasting was different in both WAT depots. For example, phosphoenolpyruvate carboxykinase 2 (*PCK2*), which facilitates glyceroneogenesis (Nye et al., 2008), was one of the most upregulated proteins in BAT after EODF (Figure 2E). Intriguingly, *SNCG* was increased in BAT after EODF, which is the opposite of the response observed in both WAT depots. Some cholesterol synthesis enzymes were increased in BAT after EODF, such as farnesyl pyrophosphate synthase (*FDPS*) (Figure 3B), but these changes were at least 4-fold lower compared with the EODF response in either WAT depot. Many mitochondrial proteins, including *UCP1* (Figure 7b), were among the most downregulated BAT proteins after EODF, which indicates a decrease in mitochondrial content, as described previously (Desautels and Dulos, 1988). In response to acute fasting, the BAT depot showed changes similar to scWAT, with increased abundance of *PDK4* and the mitochondrial quality control protein BCL2/adenovirus E1B 19-kDa protein-interacting protein 3 (*BNIP3*) (Tol et al., 2016; Figures 2F and 3C).

Given the upregulation of fatty acid synthesis-associated pathways in vWAT and scWAT, we examined in detail the response of key enzymes in all the associated pathways (Figure 5). Overall, we saw that vWAT and scWAT respond similarly to EODF, with significant upregulation of most enzymes shown but with scWAT having smaller changes in protein abundance. In addition, BAT generally shows no significant change in enzyme abundance or has a significant change in the opposite direction. In glycolysis, the most striking difference was for glucose transporter 4 (*SLC2a4* or *GLUT4*), which increased 4-fold after EODF in vWAT (Figure 5A; Figure S4). The pentose phosphate pathway showed more consistent induction across all depots, which is needed to provide NADPH for fatty acid synthesis (Figure 5b). Pyruvate metabolism showed large EODF-induced changes across all depots, with mitochondrial pyruvate carrier proteins 1 and 2 (*MPC1* and *MPC2*) having some of the largest changes in BAT and vWAT, respectively (Figure 5C;

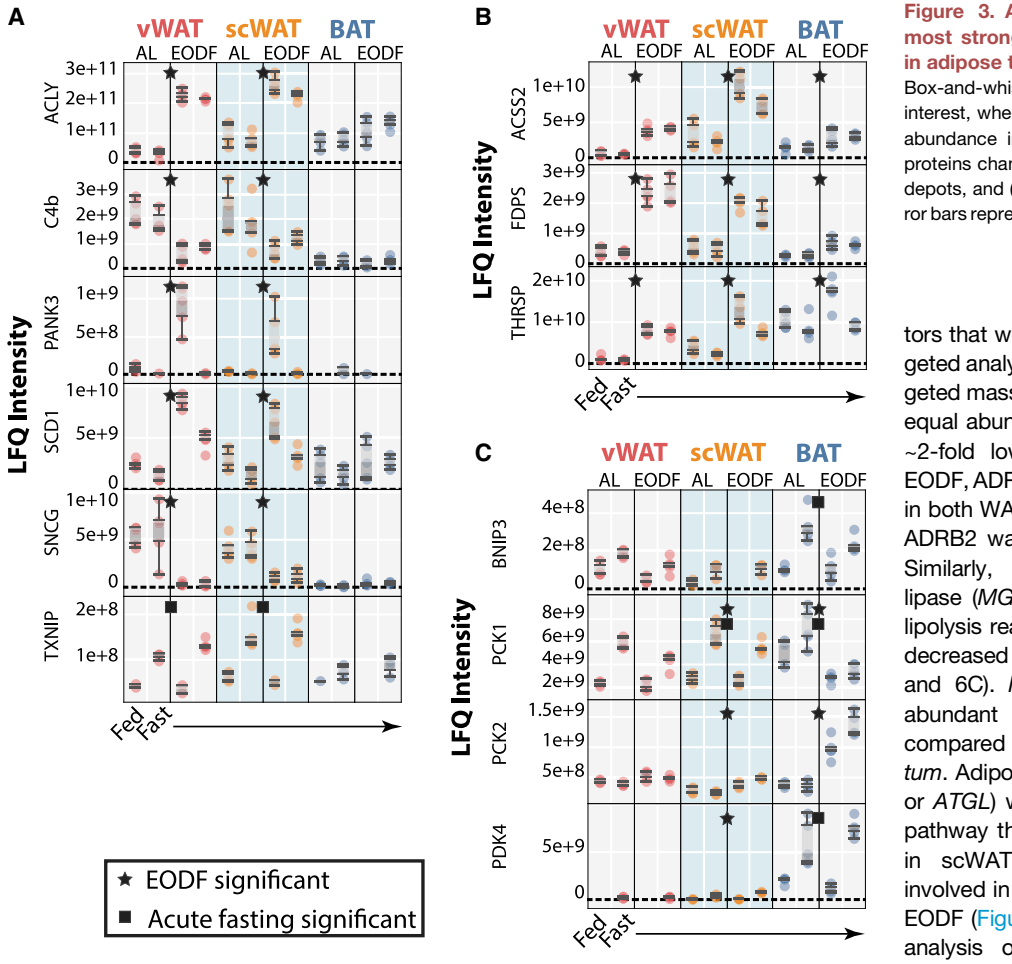

Figure 3. Analysis of proteins regulated most strongly by EODF and acute fasting in adipose tissue

Box-and-whisker plots are shown for proteins of interest, where each point represents the protein abundance in an individual mouse. Shown are proteins changing in (A) both WAT depots, (B) all depots, and (C) subcutaneous WAT and BAT. Error bars represent 1.5 times the interquartile range.

Figure S4). The TCA cycle, CoA synthesis, and fatty acid synthesis pathway enzymes again showed consistent upregulation after EODF in both WAT depots, including the key enzymes acetyl-CoA carboxylase 1 (*ACACA*), citrate synthase (*CS*), and fatty acid synthase (*FASN*) (Figure S4). In contrast, *ACACA* and *FASN* were not altered significantly in the BAT depot after EODF.

EODF triggers lipolysis resistance

In the acute fasting response, catecholamines are released through the actions of the sympathetic nervous system, which signal adipose depots to increase lipolysis and release free fatty acids for other organs to use (Figure 6A). We examined the response of this pathway to EODF and observed that the major white adipose catecholamine receptor, the β3-adrenergic receptor (*ADRB3*), was decreased ~4 fold in vWAT after EODF (Figures 6B and 6C) but was not detected in the other two depots. To improve ADRB3 detection across depots, we performed targeted LC-MS/MS analysis (Figure 6D; Figure S5; Table S4). This confirmed that ADRB3 was most abundant in vWAT and that EODF significantly decreased its abundance. Furthermore, it showed that ADRB3 was decreased in scWAT but at a much lower magnitude. This effect was not seen in BAT, where ADRB3 abundance was the lowest. The other β-adrenergic receptors that were not detected by our untargeted analysis were also examined by targeted mass spectrometry. ADRB1 had an equal abundance in both WATs and was ~2-fold lower in BAT. In response to EODF, ADRB1 abundance was decreased in both WATs but did not change in BAT. ADRB2 was not detected in any depot. Similarly, in vWAT, monoacylglycerol lipase (*MGLL*), which catalyzes the final lipolysis reaction to release glycerol, was decreased 2-fold by EODF (Figures 6B and 6C). *MGLL* was also ~2-fold less abundant overall in scWAT and BAT compared with vWAT of mice fed *ad libitum*. Adipose triglyceride lipase (*PNPLA2* or *ATGL*) was the only protein from this pathway that was increased significantly in scWAT, and no proteins directly involved in lipolysis changed in BAT after EODF (Figures 6B and 6C). Western blot analysis of *ADRB3* protein in vWAT showed an ~5-fold decrease in abundance after EODF (Figure 6E), confirming the observed decrease from the proteomics analysis. Activation of lipolytic signaling by ADRB3 triggers a phosphorylation cascade through protein kinase A (*PKA*), leading to phosphorylation of S660 on hormone-sensitive lipase (*HSL*). In animals fed *ad libitum*, HSL S660 phosphorylation in vWAT increased ~7.5-fold in mice in the fasted state compared with mice in the fed state (Figure 6E; Figure S6). In EODF animals, this response was completely blunted, with no significant increase in *HSL* S660 phosphorylation in the fasted state; there was also no significant difference in *HSL* S660 phosphorylation between EODF and AL mice in the fed state. The lipolytic potential of vWAT after EODF was tested *ex vivo*; fat explants from EODF and AL mice in the fed state were stimulated with CL-316,243, a potent ADRB3 agonist, and free glycerol release was measured as a readout of lipolytic activity (Figure 6F). This stimulation showed a ubiquitous decrease in lipolysis in vWAT from EODF mice, with the greatest decrease in lipolysis at higher doses of CL-316,243. Last, to further investigate the functional effect of EODF-induced lipolysis downregulation in vWAT, we measured plasma levels of non-esterified fatty acids (NEFA), which showed that EODF decreased the magnitude of NEFA release by 2-fold and that EODF mice in the fed state had higher plasma NEFAs than mice fed *ad libitum* in the fed state (Figure 6G).

CellPress
OPEN ACCESS

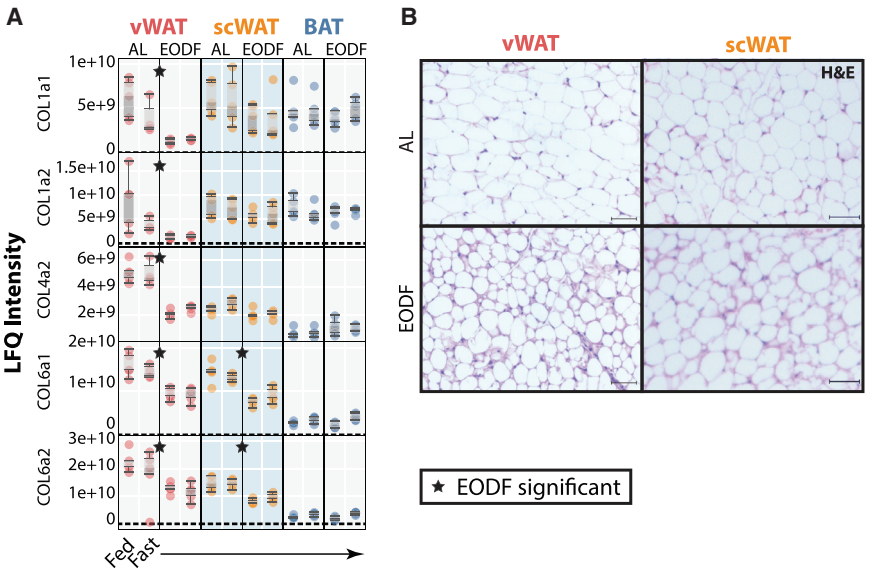

Figure 4. vWAT has reduced ECM collagen proteins in response to EODF

(A) Box-and-whisker plots are shown for proteins of interest. Each point represents the protein abundance in an individual mouse. Black stars represent diet significance and black squares represent harvest state significance ($p < 0.05$) in that tissue. Error bars represent 1.5 times the interquartile range.

(B) Adipose tissue sections stained with hematoxylin and eosin. Scale bars, 50 μm. Images are representative of 10 biological replicates per condition.

The proteomics dataset presented here not only provides an unbiased analysis of the response to intermittent and acute fasting within each depot but can also be used to look for proteins of much higher abundance in one depot versus the others. To identify these proteins, we calculated the fold change in protein abundance between adipose depots (Table S1). Several adipose-depot-enriched proteins that were up- or downregulated by EODF in a specific depot are highlighted in Figure 7. Retinaldehyde dehydrogenase 1 (*ALDH1a1*) was ~4-fold more abundant in vWAT than in the other depots, as described previously (Kiefer et al., 2012), and decreased ~2-fold in response to EODF (Figure 7A). Two other vWAT-enriched proteins that are involved in cyclic AMP (cAMP) and cyclic guanosine monophosphate (cGMP) stimulation, A-kinase anchor protein 12 (*AKAP12*) and natriuretic peptide receptor 3 (*NPR3*), were strongly downregulated by EODF so that their abundance was similar to that of scWAT. Acid ceramidase 1 (*ASAH1*) was enriched in scWAT compared with vWAT and was decreased significantly by 2-fold only in fed animals on an EODF diet. *UCP1*, a marker of adipocyte browning and mitochondrial uncoupling, was more than 100 times more abundant in BAT from animals fed *ad libitum* compared with either WAT depot (Figure 7B). In response to EODF, *UCP1* abundance decreased by ~4-fold in BAT, whereas in scWAT, EODF increased *UCP1* abundance by ~6-fold. However, even after this modulation of both depots by EODF, the protein abundance of *UCP1* in BAT was ~50-fold higher than in scWAT.

DISCUSSION

In this study, we performed unbiased mass spectrometry-based proteomics analyses to elucidate adipose-depot-specific responses to EODF in mice. These analyses uncovered substantial differences in the EODF response between all three adipose depots. In general, vWAT showed more proteins significantly altered by the EODF diet with the largest fold changes in protein abundance compared with scWAT and that BAT had a distinct inverse response to EODF. These analyses resulted in four key findings. First, vWAT of EODF mice had a 4-fold decrease in the *ADRB3* protein, needed for lipolysis induction, leading to decreased phosphorylation of *HSL* and decreased NEFA release into plasma during acute fasting of EODF mice. Second, both WAT depots in EODF mice displayed ~2-fold increases in abundance of mitochondrial proteins after EODF, but only scWAT showed an increase in *UCP1* protein abundance. Third, an increased abundance of fatty acid synthesis enzymes was observed after EODF in both WAT depots but not BAT. EODF also induced the nutrient uptake pathways upstream of fatty acid synthesis, including glycolysis and pyruvate metabolism, in both WAT depots. Last, there was a significant reduction in ECM proteins of vWAT after EODF. These findings show how the adipose depots have adapted to the EODF regimen to preserve the lipid store, with the most striking changes occurring in the vWAT depot to downregulate the lipolysis pathway and induce expression of pathways needed for fatty acid synthesis. These data provide a comparative proteomics analysis of adipose depot-specific responses after EODF and offer insights into changes that may contribute to the improved metabolic benefits associated with IF (Figure S7). This proteomic resource is provided as a free web-based interactive visualization for the research community (https://www.larancelab.com/fat-eodf), and a short tutorial is provided (Methods S1).

We observed by untargeted mass spectrometry that the EODF intervention leads to a decreased abundance of *ADRB3* protein by 4-fold in vWAT. In scWAT and BAT, *ADRB3* protein abundance in mice fed *ad libitum* was ~10-fold less than in vWAT, which agrees with previous mRNA observations (Fujimoto et al., 2019), but the lower abundance prevented consistent quantification by untargeted mass spectrometry. To further elucidate the differences in β-adrenergic receptors between depots, targeted mass spectrometry analysis was performed on *ADRB1*, *ADRB2*, and *ADRB3*. In response to EODF, ADRB1 abundance was approximately halved in both WATs and did not change in BAT in response to EODF. We observed similar results in the untargeted analysis for ADRB3 in vWAT, whereas scWAT followed a similar trend as vWAT but at a much lower magnitude. We did not detect ADRB2 in any depot. Interestingly, ADRB3 had the lowest abundance in BAT and was not EODF responsive. Previous studies examining adrenergic receptor abundance in BAT

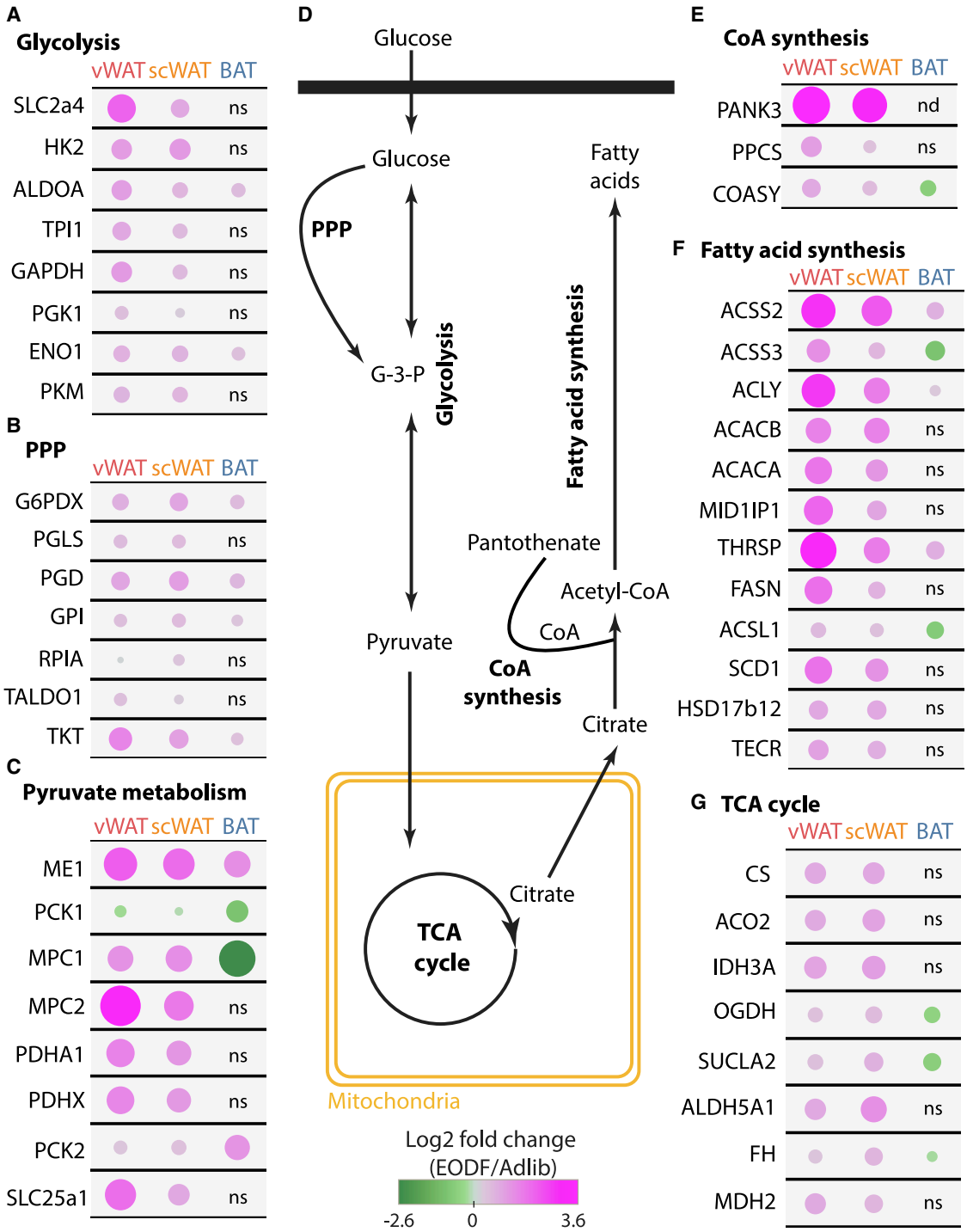

Figure 5. EODF upregulates catabolic and fatty acid synthesis pathways in WAT but not BAT

(A–C and E–G) Each circle represents the Log_2 fold change of the EODF/*ad libitum* response (n = 5 per condition). Pink represents a positive fold change and green a negative fold change; size also correlates with fold change. Proteins that were not significant ($p > 0.05$) were not included and are represented by ns (not significant). Proteins that were not detected in that tissue are represented by nd (not detected).

(D) Schematic of nutrient uptake and integration into fatty acid synthesis in adipose tissues.

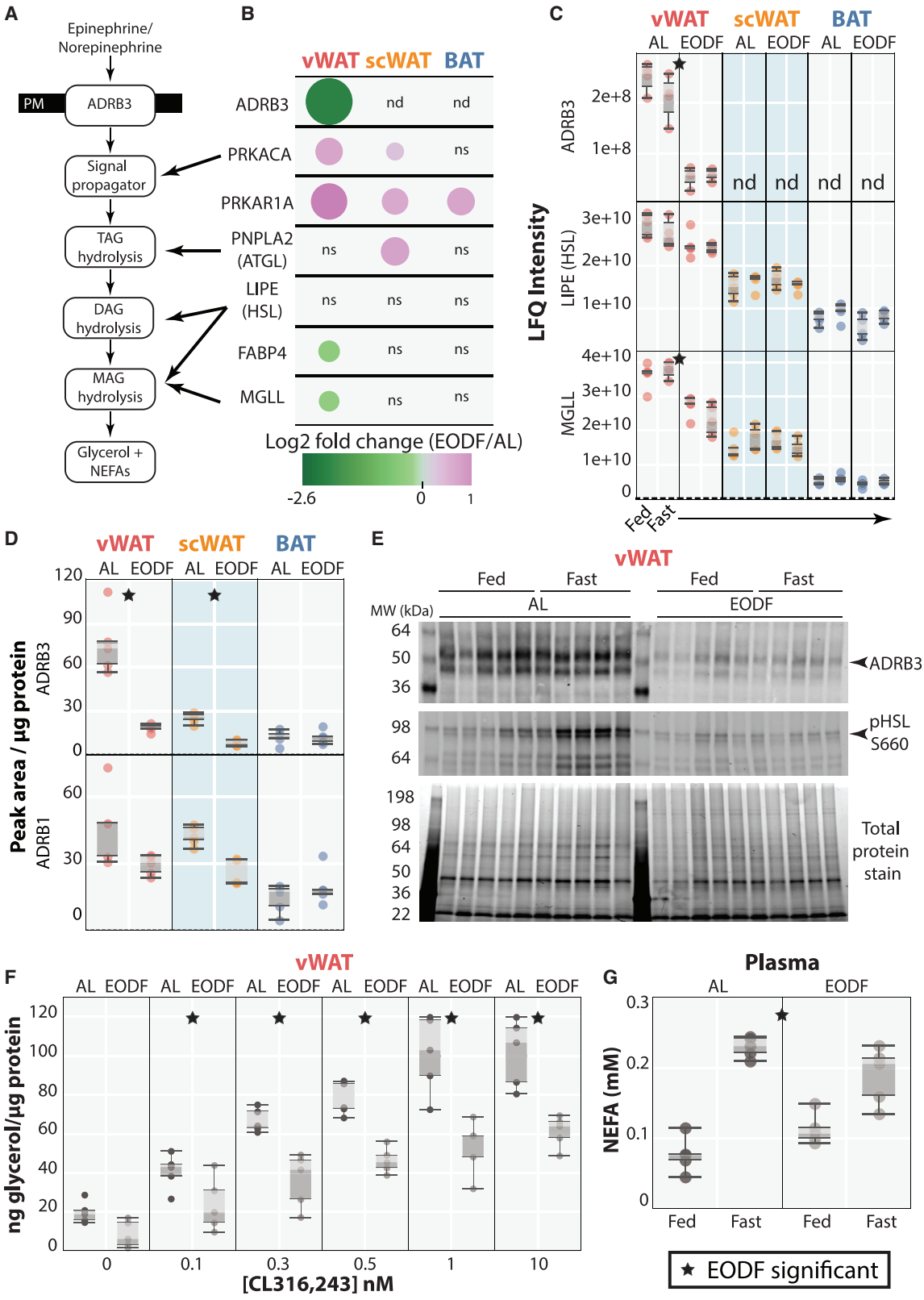

(legend on next page)

have demonstrated that ADRB2 is the most abundant mRNA in human tissue (Blondin et al., 2020), whereas ADRB3 is the most abundant in mice (Cannon and Nedergaard, 2004). Furthermore, a null mutation in ADRB3 in mice largely impairs the stimulated lipolytic activity of BAT (Preitner et al., 1998). These data and other reports demonstrate that, although BAT can perform lipolysis, it is not necessary for responding to IF or cold exposure, where knockout of key lipolysis or lipogenesis did not inhibit BAT thermogenesis (Chitraju et al., 2020; Shin et al., 2017). In these situations, BAT relies more on free fatty acids and glucose from WAT. Comparing WAT depots, previous data have demonstrated that vWAT is the most catecholamine-sensitive adipose depot (Arner, 2005; Fujimoto et al., 2019; Rebuffé-Scrive et al., 1989). Coupled with the decreased *ADRB3* protein abundance after EODF in vWAT, we observed a decrease in fasting-induced phosphorylation of *HSL* at S660, an essential site for lipolytic activation. *Ex vivo* analysis of the lipolytic potential of vWAT using the ADRB3 agonist CL-316,243 demonstrated a generalized decrease in lipolysis that was exacerbated with greater CL doses. We propose that the repeated fasting bouts during EODF, each of which leads to a marked increase in vWAT lipolysis, generates negative feedback that decreases *ADRB3* protein abundance. This is reflected in the significantly lower induction of plasma NEFA abundance in EODF mice after an acute fasting bout compared with animals fed *ad libitum*. This negative feedback response would help to preserve vWAT lipid reserves from depletion during EODF. The pathways that underpin this negative feedback regulation of *ADRB3* remain unclear. Unlike other adrenergic G protein-coupled receptors, *ADRB3* is resistant to desensitization, where overstimulation with a receptor agonist induces negative feedback by phosphorylation of the receptor (Granneman and Lahners, 1995; Hutchinson et al., 2000). However, previous IF studies have shown decreased levels of *ADRB3* mRNA after IF in vWAT (Kim et al., 2019) and scWAT (Li et al., 2017), suggesting that transcriptional modulation is key. How *ADRB3* transcription is regulated is not well understood. SHOX2 has recently been identified as an upstream transcription factor that displays adipose-depot-specific expression (Lee et al., 2013), and when overexpressed in adipocytes, their sensitivity to lipolysis induction was decreased concomitant with decreased *ADRB3* mRNA and protein abundance (Lee et al., 2013). However, the mechanism behind SHOX2 regulation of ADRB3 transcription is unknown, and we observed no direct evidence of SHOX2 activity. Therefore, further research is required to determine the exact nature of the negative feedback inhibition mechanism leading to downregulation of ADRB3.

We observed a widespread increase in the abundance of mitochondrial proteins in vWAT and scWAT after EODF, where half of the 500 proteins most upregulated by EODF in vWAT were mitochondrial. When comparing the WAT depots, vWAT, on average, displayed the largest increase in mitochondrial proteins compared with scWAT. Conversely, BAT had a general decrease in mitochondrial protein content after EODF, which included downregulation of *UCP1* protein abundance. Accumulation of mitochondria in WAT is one of several phenotypes in the process of "browning," which is generally associated with uncoupling potential, heat production, and greater energy expenditure (Bartelt and Heeren, 2014; Chouchani and Kajimura, 2019; Chouchani et al., 2019; Harms and Seale, 2013; Kajimura et al., 2015; Nedergaard and Cannon, 2014). Prior studies of IF in mice have demonstrated increased scWAT browning, including increased *UCP1* protein expression, which contributes to amelioration of insulin resistance, obesity, and metabolic disease (Kim et al., 2017; Li et al., 2017). Similarly, vWAT from these animals had indications of browning, based on an increase in *UCP1* mRNA in obese mice on an IF diet (Kim et al., 2017). However, a follow-up study where *ob/ob* mice were placed on an isocaloric IF diet did not show similar UCP1 upregulation in vWAT (Kim et al., 2019). In this study, we observed mitochondrial protein induction in both WAT depots but a detectable increase in *UCP1* protein abundance only in scWAT. This suggests that *UCP1* is not central to the increased mitochondrial protein content seen in WAT depots during IF and that the central purpose of the observed mitogenesis is not necessarily *UCP1*-dependent thermogenesis. Similarly, the induced *UCP1* protein levels seen in EODF scWAT are 50-fold lower than that of the BAT depot, suggesting a less important role in thermogenesis and increased energy expenditure for *UCP1* in scWAT. This correlates with previous studies using selective deletion of *UCP1*-positive beige adipocytes in WAT of mice, which demonstrated no change in body temperature and minimal changes in energy expenditure (<5%) at room temperature (Bond and Ntambi, 2018; Challa et al., 2020; Enerbäck et al., 1997). We propose that the EODF-induced increase in mitochondrial protein content may have a different function, such as promoting the observed increase in fatty acid synthesis pathways. Mitochondria play a

Figure 6. EODF negatively regulates lipolysis surface receptor and downstream effectors in vWAT

(A) Schematic of lipolysis induction, signal transduction, and the individual steps required to break down TAG in adipose tissue. Black stars represent diet significance and black squares represent harvest state significance ($p < 0.05$) in that tissue.

(B) Each circle represents the Log_2 fold change of the EODF/*ad libitum* response (n = 5 per condition). Pink represents a positive fold change and green a negative fold change; size also correlates with fold change. Proteins that were not significant ($p > 0.05$) were not included and are represented by ns. Proteins that were not detected in that tissue are represented by nd.

(C) Box-and-whisker plots are shown for proteins of interest detected by untargeted mass spectrometry. Each point represents the protein abundance in an individual mouse (n = 5).

(D) Box-and-whisker plots are shown for proteins of interest detected by targeted mass spectrometry. Signal intensity was normalized to peptide concentration. Each point represents the protein abundance in an individual mouse (n = 5).

(E) Western blot analysis of the lipolysis pathway.

(F) *In vitro* lipolysis assay using fresh visceral adipose tissue exposed to varying concentrations of the ADRB3 agonist CL and their lipolytic potential, analyzed by glycerol release in a colorimetry assay. Each circle represents an individual data point from 2 pooled mice (n = 5 from 10 mice).

(G) Box-and-whisker plots for plasma non-esterified fatty acids (NEFAs), measured by colorimetry assay. Each circle represents measurement of an individual animal (n = 5). For all box-and-whisker plots, error bars represent 1.5 times the interquartile range.

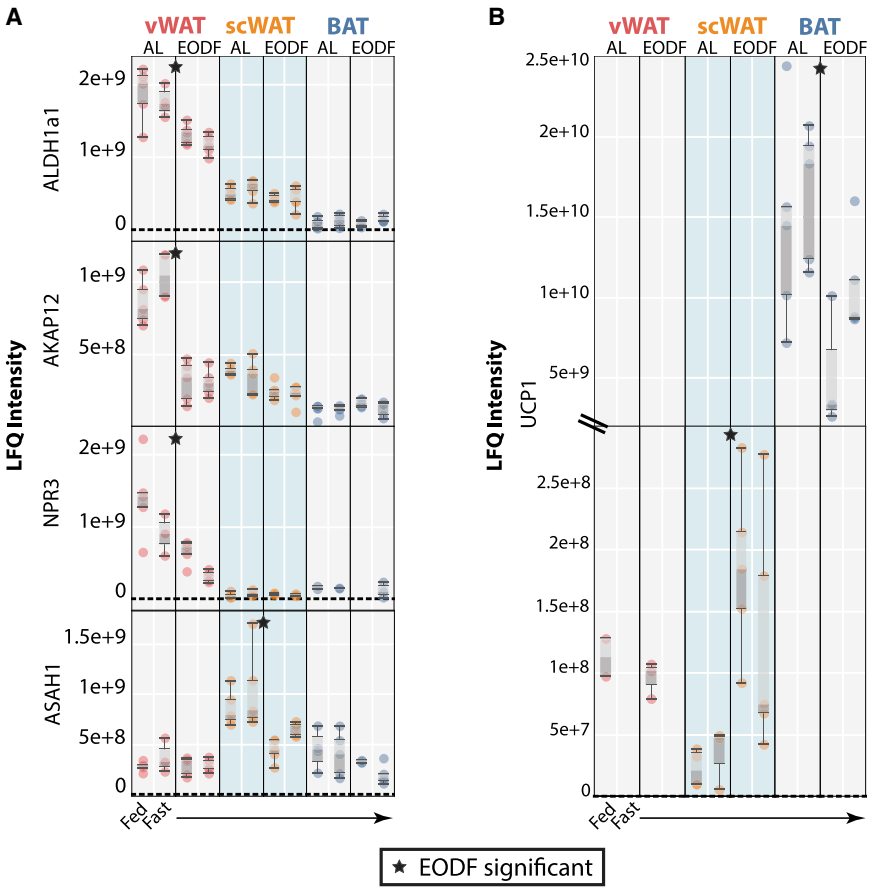

Figure 7. Proteomics analysis reveals adipose-depot-specific responses for individual proteins

(A) Box-and-whisker plots are shown for proteins of interest. (B) Box-and-whisker plot for UCP1 with split y-axis. For all plots, each point represents the protein abundance in an individual mouse (n = 5). Black stars represent diet significance and black squares represent harvest state significance ($p < 0.05$) in that tissue. Error bars represent 1.5 times the interquartile range.

key role in converting pyruvate to citrate, and there are several steps in this pathway that may be rate limiting, such as pyruvate import into the mitochondria and pyruvate dehydrogenase activity (Flatt, 1970; Held et al., 2018). Again, this would help protect lipid stores from depletion from the increased lipolytic demand during EODF. One mechanism that may mediate this increase in mitochondrial protein content is *PPARgamma* activation by FFAs produced during lipolysis, which would subsequently induce lipogenic gene expression (Mottillo et al., 2014).

Fibrosis of adipose tissue through accumulation of ECM proteins has been heavily correlated with poor metabolic health (Chouchani and Kajimura, 2019; Sun et al., 2013). In humans, scWAT fibrosis has been most strongly correlated with poor health outcomes, but in rodents, vWAT and scWAT fibrosis is associated with poor health outcomes (Divoux et al., 2010; Hasegawa et al., 2018; Muir et al., 2016). We have demonstrated that EODF reduces the abundance of several ECM proteins specifically in vWAT. Most interesting is the reduction of collagen types IV and VI because these are the main contributors to ECM expansion during obesity (Sun et al., 2014). Histopathological imaging using picrosirius red staining did not show any change in staining distribution or intensity between vWAT of mice fed *ad libitum* and EODF mice, which was most likely due to detection of all collagen subtypes. During obesity, increased ECM protein content of adipose tissue is observed, reducing its potential to expand and store more triacylglycerol (TAG). WAT with reduced lipid storage potential leads to accumulation of lipids in other organs, such as the liver, which contributes to liver fibrosis and increased cancer risk (Ekstedt et al., 2015; Fabbrini et al., 2010; Sun et al., 2013; Younossi et al., 2016). This makes IF an attractive option for treatment and reduction of obesity as well as reducing the effect of its co-morbidities. Furthermore, the cleavage of collagen VI produces the adipokine endotrophin, which can promote endothelial cell migration as well as recruitment and infiltration of macrophages into a fat pad (Sun et al., 2014, 2017). Therefore, by reducing these specific collagens in vWAT, there is a reduction in inflammatory potential that can improve metabolic health by reducing immune cell infiltration. This, in turn, can act to improve the insulin sensitivity of the fat pad. Future studies to examine whether IF reduces ECM accumulation in an obesity model where there is significant adipocyte fibrosis would help prove the efficacy of this approach.

Our analysis of the adipose depot responses to EODF identified many significant changes that were enriched specifically in only one adipose depot. *ALDH1a1* was 4-fold higher in abundance in vWAT from mice fed *ad libitum* and decreased by half in response to EODF. This agrees with a previous study of *ALDH1a1* demonstrating that knockout animals display increased browning of vWAT through upregulation of *UCP1* and other BAT-related proteins (Kiefer et al., 2012); this was not seen in our study. There was alignment with increased mitochondrial content, and the difference may lie in downregulation of *ALDH1a1* in our study versus knockout in the previous study. *AKAP12* was enriched in vWAT compared with other depots and was downregulated by EODF. *AKAP12* is an anchor protein that helps coordinate receptor signal propagation to downstream effectors, including *PKA* (Ibarrola et al., 2018). Its downregulation after EODF would decrease *PKA* activation (Guillory et al., 2013; Rababa'h et al., 2014). This suggests that *AKAP12* contributes to the decreased lipolytic activity seen in our EODF model and may have an association with *ADRB3* signaling. Indeed, *AKAP12* has been studied previously in the context of cardiomyocytes, where it has been reported to bind to the β2-adrenergic receptor (*ADRB2*) and *PKA*, functionally coupling the receptor to downstream signaling pathways, which were

reduced greatly in *AKAP12* knockout mice (Fan et al., 2019; Guillory et al., 2013; Rababa'h et al., 2014). We suggest that *AKAP12* may play a role in ADRB3 signaling in adipose tissue and that its downregulation after EODF in vWAT would contribute to the reduction in lipolytic potential.

This study provides an unbiased proteomics analysis of the response to IF and acute fasting in multiple adipose depots, highlighting changes in key metabolic pathways that may improve metabolic health. These findings include decreased abundance of the lipolysis receptor *ADRB3* and its downstream signaling in vWAT after EODF, likely to help protect the lipid store from depletion. We also observed a consistent increase in mitochondrial protein content in both WAT depots after EODF, which, we propose, facilitates the increase in fatty acid synthesis pathways we observed in both WAT depots after EODF. Unexpectedly, we observed a decrease in ECM proteins in the visceral white adipose depot of EODF-treated mice, which is correlated with decreased inflammation and improved insulin sensitivity. Future studies characterizing the response to IF in the adipose depots of healthy or obese individuals would demonstrate the conservation of these responses. Similarly, pharmacological perturbation of the pathways identified here, regulated by EODF, could provide beneficial metabolic benefits independent of fasting.

STAR★METHODS

Detailed methods are provided in the online version of this paper and include the following:

- KEY RESOURCES TABLE
- RESOURCE AVAILABILITY
  - Lead contact
  - Materials availability
  - Data and code availability
- EXPERIMENTAL MODEL AND SUBJECT DETAILS
  - Mice
  - Intermittent fasting model
- METHOD DETAILS
  - Determination of glucose tolerance
  - Body composition analysis
  - Tissue collection
  - Non-esterified fatty acid determination in plasma
  - Lipolysis assay
  - Histopathology
  - Sample preparation of adipose tissue for protein mass-spectrometry
  - Chloroform-methanol precipitation
  - Trypsin digestion for proteome analysis
  - High pH reverse-phase LC fractionation
  - Protein LC-MS/MS and spectra analysis
  - Targeted mass spectrometry of beta-adrenergic receptors
- QUANTIFICATION AND STATISTICAL ANALYSIS

SUPPLEMENTAL INFORMATION

Supplemental information can be found online at https://doi.org/10.1016/j.celrep.2021.108804.

ACKNOWLEDGMENTS

M.L. is a Cancer Institute New South Wales Future Research Leader Fellow. This work was supported by a grant from the NHMRC (GNT1120475). D.E.J. is an NHMRC Senior Principal Research Fellow. We thank SydneyMS for providing the instrumentation used in this study.

AUTHOR CONTRIBUTIONS

M.L. conceived and supervised the project. D.J.H., M.C., R.C., and M.L. performed all animal experiments. D.J.H. and M.L. performed the proteomics experiments and data analyses. K.C.C., D.E.J., and J.S. performed the lipolysis assay. D.J.H. and M.L. wrote the manuscript.

DECLARATION OF INTERESTS

The authors declare no competing interests.

Received: July 20, 2020
Revised: January 22, 2021
Accepted: February 5, 2021
Published: March 2, 2021

REFERENCES

Anson, R.M., Guo, Z., de Cabo, R., Iyun, T., Rios, M., Hagepanos, A., Ingram, D.K., Lane, M.A., and Mattson, M.P. (2003). Intermittent fasting dissociates beneficial effects of dietary restriction on glucose metabolism and neuronal resistance to injury from calorie intake. Proc. Natl. Acad. Sci. USA *100*, 6216–6220.

Arany, Z., Foo, S.Y., Ma, Y., Ruas, J.L., Bommi-Reddy, A., Girnun, G., Cooper, M., Laznik, D., Chinsomboon, J., Rangwala, S.M., et al. (2008). HIF-independent regulation of VEGF and angiogenesis by the transcriptional coactivator PGC-1alpha. Nature *451*, 1008–1012.

Arner, P. (2005). Human fat cell lipolysis: biochemistry, regulation and clinical role. Best Pract. Res. Clin. Endocrinol. Metab. *19*, 471–482.

Barnosky, A.R., Hoddy, K.K., Unterman, T.G., and Varady, K.A. (2014). Intermittent fasting vs daily calorie restriction for type 2 diabetes prevention: a review of human findings. Transl. Res. *164*, 302–311.

Bartelt, A., and Heeren, J. (2014). Adipose tissue browning and metabolic health. Nat. Rev. Endocrinol. *10*, 24–36.

Blondin, D.P., Nielsen, S., Kuipers, E.N., Severinsen, M.C., Jensen, V.H., Miard, S., Jespersen, N.Z., Kooijman, S., Boon, M.R., Fortin, M., et al. (2020). Human Brown Adipocyte Thermogenesis Is Driven by β2-AR Stimulation. Cell Metab. *32*, 287–300.e7.

Bond, L.M., and Ntambi, J.M. (2018). UCP1 deficiency increases adipose tissue monounsaturated fatty acid synthesis and trafficking to the liver. J. Lipid Res. *59*, 224–236.

Cannon, B., and Nedergaard, J. (2004). Brown adipose tissue: function and physiological significance. Physiol. Rev. *84*, 277–359.

Chaix, A., Zarrinpar, A., Miu, P., and Panda, S. (2014). Time-restricted feeding is a preventative and therapeutic intervention against diverse nutritional challenges. Cell Metab. *20*, 991–1005.

Challa, T.D., Dapito, D.H., Kulenkampff, E., Kiehlmann, E., Moser, C., Straub, L., Sun, W., and Wolfrum, C. (2020). A Genetic Model to Study the Contribution of Brown and Brite Adipocytes to Metabolism. Cell Rep. *30*, 3424–3433.e4.

Chitraju, C., Fischer, A.W., Farese, R.V., Jr., and Walther, T.C. (2020). Lipid Droplets in Brown Adipose Tissue Are Dispensable for Cold-Induced Thermogenesis. Cell Rep. *33*, 108348.

Chouchani, E.T., and Kajimura, S. (2019). Metabolic adaptation and maladaptation in adipose tissue. Nat. Metab. *1*, 189–200.

Chouchani, E.T., Kazak, L., and Spiegelman, B.M. (2019). New Advances in Adaptive Thermogenesis: UCP1 and Beyond. Cell Metab. *29*, 27–37.

Cox, J., and Mann, M. (2008). MaxQuant enables high peptide identification rates, individualized p.p.b.-range mass accuracies and proteome-wide protein quantification. Nat. Biotechnol. *26*, 1367–1372.

Cox, J., Neuhauser, N., Michalski, A., Scheltema, R.A., Olsen, J.V., and Mann, M. (2011). Andromeda: a peptide search engine integrated into the MaxQuant environment. J. Proteome Res. *10*, 1794–1805.

Cox, J., Hein, M.Y., Luber, C.A., Paron, I., Nagaraj, N., and Mann, M. (2014). Accurate proteome-wide label-free quantification by delayed normalization and maximal peptide ratio extraction, termed MaxLFQ. Mol. Cell. Proteomics *13*, 2513–2526.

Desautels, M., and Dulos, R.A. (1988). Effects of repeated cycles of fasting-refeeding on brown adipose tissue composition in mice. Am. J. Physiol. *255*, E120–E128.

Després, J.P. (2012). Body fat distribution and risk of cardiovascular disease: an update. Circulation *126*, 1301–1313.

Després, J.P., and Lemieux, I. (2006). Abdominal obesity and metabolic syndrome. Nature *444*, 881–887.

Divoux, A., Tordjman, J., Lacasa, D., Veyrie, N., Hugol, D., Aissat, A., Basdevant, A., Guerre-Millo, M., Poitou, C., Zucker, J.D., et al. (2010). Fibrosis in human adipose tissue: composition, distribution, and link with lipid metabolism and fat mass loss. Diabetes *59*, 2817–2825.

Dunn, T.N., Akiyama, T., Lee, H.W., Kim, J.B., Knotts, T.A., Smith, S.R., Sears, D.D., Carstens, E., and Adams, S.H. (2015). Evaluation of the synuclein-γ (SNCG) gene as a PPARγ target in murine adipocytes, dorsal root ganglia somatosensory neurons, and human adipose tissue. PLoS ONE *10*, e0115830.

Ekstedt, M., Hagström, H., Nasr, P., Fredrikson, M., Stål, P., Kechagias, S., and Hultcrantz, R. (2015). Fibrosis stage is the strongest predictor for disease-specific mortality in NAFLD after up to 33 years of follow-up. Hepatology *61*, 1547–1554.

Enerbäck, S., Jacobsson, A., Simpson, E.M., Guerra, C., Yamashita, H., Harper, M.E., and Kozak, L.P. (1997). Mice lacking mitochondrial uncoupling protein are cold-sensitive but not obese. Nature *387*, 90–94.

Fabbrini, E., Sullivan, S., and Klein, S. (2010). Obesity and nonalcoholic fatty liver disease: biochemical, metabolic, and clinical implications. Hepatology *51*, 679–689.

Fan, Q., Yin, X., Rababa'h, A., Diaz Diaz, A., Wijaya, C.S., Singh, S., Suryavanshi, S.V., Vo, H.H., Saeed, M., Zhang, Y., and McConnell, B.K. (2019). Absence of gravin-mediated signaling inhibits development of high-fat diet-induced hyperlipidemia and atherosclerosis. Am. J. Physiol. Heart Circ. Physiol. *317*, H793–H810.

Farb, M.G., and Gokce, N. (2015). Visceral adiposopathy: a vascular perspective. Horm. Mol. Biol. Clin. Investig. *21*, 125–136.

Flatt, J.P. (1970). Conversion of carbohydrate to fat in adipose tissue: an energy-yielding and, therefore, self-limiting process. J. Lipid Res. *11*, 131–143.

Fox, C.S., Massaro, J.M., Hoffmann, U., Pou, K.M., Maurovich-Horvat, P., Liu, C.Y., Vasan, R.S., Murabito, J.M., Meigs, J.B., Cupples, L.A., et al. (2007). Abdominal visceral and subcutaneous adipose tissue compartments: association with metabolic risk factors in the Framingham Heart Study. Circulation *116*, 39–48.

Fujimoto, Y., Hashimoto, O., Shindo, D., Sugiyama, M., Tomonaga, S., Murakami, M., Matsui, T., and Funaba, M. (2019). Metabolic changes in adipose tissues in response to β_3 -adrenergic receptor activation in mice. J. Cell. Biochem. *120*, 821–835.

Goodrick, C.L., Ingram, D.K., Reynolds, M.A., Freeman, J.R., and Cider, N. (1990). Effects of intermittent feeding upon body weight and lifespan in inbred mice: interaction of genotype and age. Mech. Ageing Dev. *55*, 69–87.

Granneman, J.G., and Lahners, K.N. (1995). Regulation of mouse beta 3-adrenergic receptor gene expression and mRNA splice variants in adipocytes. Am. J. Physiol. *268*, C1040–C1044.

Guilherme, A., Henriques, F., Bedard, A.H., and Czech, M.P. (2019). Molecular pathways linking adipose innervation to insulin action in obesity and diabetes mellitus. Nat. Rev. Endocrinol. *15*, 207–225.

Guillory, A.N., Yin, X., Wijaya, C.S., Diaz Diaz, A.C., Rababa'h, A., Singh, S., Atrooz, F., Sadayappan, S., and McConnell, B.K. (2013). Enhanced cardiac function in Gravin mutant mice involves alterations in the β-adrenergic receptor signaling cascade. PLoS ONE *8*, e74784.

Habegger, K.M., Heppner, K.M., Geary, N., Bartness, T.J., DiMarchi, R., and Tschöp, M.H. (2010). The metabolic actions of glucagon revisited. Nat. Rev. Endocrinol. *6*, 689–697.

Harms, M., and Seale, P. (2013). Brown and beige fat: development, function and therapeutic potential. Nat. Med. *19*, 1252–1263.

Harney, D.J., Hutchison, A.T., Hatchwell, L., Humphrey, S.J., James, D.E., Hocking, S., Heilbronn, L.K., and Larance, M. (2019a). Proteomic Analysis of Human Plasma during Intermittent Fasting. J. Proteome Res. *18*, 2228–2240.

Harney, D.J., Hutchison, A.T., Su, Z., Hatchwell, L., Heilbronn, L.K., Hocking, S., James, D.E., and Larance, M. (2019b). Small-protein Enrichment Assay Enables the Rapid, Unbiased Analysis of Over 100 Low Abundance Factors from Human Plasma. Mol. Cell. Proteomics *18*, 1899–1915.

Hasegawa, Y., Ikeda, K., Chen, Y., Alba, D.L., Stifler, D., Shinoda, K., Hosono, T., Maretich, P., Yang, Y., Ishigaki, Y., et al. (2018). Repression of Adipose Tissue Fibrosis through a PRDM16-GTF2IRD1 Complex Improves Systemic Glucose Homeostasis. Cell Metab. *27*, 180–194.e6.

Hatchwell, L., Harney, D.J., Cielesh, M., Young, K., Koay, Y.C., O'Sullivan, J.F., and Larance, M. (2020). Multi-omics Analysis of the Intermittent Fasting Response in Mice Identifies an Unexpected Role for HNF4α. Cell Rep. *30*, 3566–3582.e4.

Hayes, A.J., Lung, T.W., Bauman, A., and Howard, K. (2017). Modelling obesity trends in Australia: unravelling the past and predicting the future. Int. J. Obes. *41*, 178–185.

Heilbronn, L.K., Smith, S.R., Martin, C.K., Anton, S.D., and Ravussin, E. (2005). Alternate-day fasting in nonobese subjects: effects on body weight, body composition, and energy metabolism. Am. J. Clin. Nutr. *81*, 69–73.

Held, N.M., Kuipers, E.N., van Weeghel, M., van Klinken, J.B., Denis, S.W., Lombès, M., Wanders, R.J., Vaz, F.M., Rensen, P.C.N., Verhoeven, A.J., et al. (2018). Pyruvate dehydrogenase complex plays a central role in brown adipocyte energy expenditure and fuel utilization during short-term beta-adrenergic activation. Sci. Rep. *8*, 9562.

Hui, S., Cowan, A.J., Zeng, X., Yang, L., TeSlaa, T., Li, X., Bartman, C., Zhang, Z., Jang, C., Wang, L., et al. (2020). Quantitative Fluxomics of Circulating Metabolites. Cell Metab. *32*, 676–688.e4.

Huss, J.M., Kopp, R.P., and Kelly, D.P. (2002). Peroxisome proliferator-activated receptor coactivator-1alpha (PGC-1alpha) coactivates the cardiac-enriched nuclear receptors estrogen-related receptor-alpha and -gamma. Identification of novel leucine-rich interaction motif within PGC-1alpha. J. Biol. Chem. *277*, 40265–40274.

Hutchinson, D.S., Evans, B.A., and Summers, R.J. (2000). beta(3)-adrenoceptor regulation and relaxation responses in mouse ileum. Br. J. Pharmacol. *129*, 1251–1259.

Ibarrola, J., Sadaba, R., Martinez-Martinez, E., Garcia-Peña, A., Arrieta, V., Alvarez, V., Fernández-Celis, A., Gainza, A., Cachofeiro, V., Santamaria, E., et al. (2018). Aldosterone Impairs Mitochondrial Function in Human Cardiac Fibroblasts via A-Kinase Anchor Protein 12. Sci. Rep. *8*, 6801.

Kajimura, S., Seale, P., and Spiegelman, B.M. (2010). Transcriptional control of brown fat development. Cell Metab. *11*, 257–262.

Kajimura, S., Spiegelman, B.M., and Seale, P. (2015). Brown and Beige Fat: Physiological Roles beyond Heat Generation. Cell Metab. *22*, 546–559.

Kiefer, F.W., Vernochet, C., O'Brien, P., Spoerl, S., Brown, J.D., Nallamshetty, S., Zeyda, M., Stulnig, T.M., Cohen, D.E., Kahn, C.R., and Plutzky, J. (2012). Retinaldehyde dehydrogenase 1 regulates a thermogenic program in white adipose tissue. Nat. Med. *18*, 918–925.

Kim, K.H., Kim, Y.H., Son, J.E., Lee, J.H., Kim, S., Choe, M.S., Moon, J.H., Zhong, J., Fu, K., Lenglin, F., et al. (2017). Intermittent fasting promotes adipose thermogenesis and metabolic homeostasis via VEGF-mediated alternative activation of macrophage. Cell Res. *27*, 1309–1326.

Kim, Y.H., Lee, J.H., Yeung, J.L., Das, E., Kim, R.Y., Jiang, Y., Moon, J.H., Jeong, H., Thakkar, N., Son, J.E., et al. (2019). Thermogenesis-independent metabolic benefits conferred by isocaloric intermittent fasting in ob/ob mice. Sci. Rep. *9*, 2479.

Kopelman, P.G. (2000). Obesity as a medical problem. Nature *404*, 635–643.

Kwon, H., Kim, D., and Kim, J.S. (2017). Body Fat Distribution and the Risk of Incident Metabolic Syndrome: A Longitudinal Cohort Study. Sci. Rep. *7*, 10955.

Lafontan, M., and Langin, D. (2009). Lipolysis and lipid mobilization in human adipose tissue. Prog. Lipid Res. *48*, 275–297.

Lee, K.Y., Yamamoto, Y., Boucher, J., Winnay, J.N., Gesta, S., Cobb, J., Blüher, M., and Kahn, C.R. (2013). Shox2 is a molecular determinant of depot-specific adipocyte function. Proc. Natl. Acad. Sci. USA *110*, 11409–11414.

Li, G., Xie, C., Lu, S., Nichols, R.G., Tian, Y., Li, L., Patel, D., Ma, Y., Brocker, C.N., Yan, T., et al. (2017). Intermittent Fasting Promotes White Adipose Browning and Decreases Obesity by Shaping the Gut Microbiota. Cell Metab. *26*, 801.

Liu, J., Fox, C.S., Hickson, D.A., May, W.D., Hairston, K.G., Carr, J.J., and Taylor, H.A. (2010). Impact of abdominal visceral and subcutaneous adipose tissue on cardiometabolic risk factors: the Jackson Heart Study. J. Clin. Endocrinol. Metab. *95*, 5419–5426.

Liu, B., Page, A.J., Hutchison, A.T., Wittert, G.A., and Heilbronn, L.K. (2019). Intermittent fasting increases energy expenditure and promotes adipose tissue browning in mice. Nutrition *66*, 38–43.

Mootha, V.K., Handschin, C., Arlow, D., Xie, X., St Pierre, J., Sihag, S., Yang, W., Altshuler, D., Puigserver, P., Patterson, N., et al. (2004). Erralpha and Gabpa/b specify PGC-1alpha-dependent oxidative phosphorylation gene expression that is altered in diabetic muscle. Proc. Natl. Acad. Sci. USA *101*, 6570–6575.

Mottillo, E.P., Balasubramanian, P., Lee, Y.H., Weng, C., Kershaw, E.E., and Granneman, J.G. (2014). Coupling of lipolysis and de novo lipogenesis in brown, beige, and white adipose tissues during chronic β3-adrenergic receptor activation. J. Lipid Res. *55*, 2276–2286.

Muir, L.A., Neeley, C.K., Meyer, K.A., Baker, N.A., Brosius, A.M., Washabaugh, A.R., Varban, O.A., Finks, J.F., Zamarron, B.F., Flesher, C.G., et al. (2016). Adipose tissue fibrosis, hypertrophy, and hyperplasia: Correlations with diabetes in human obesity. Obesity (Silver Spring) *24*, 597–605.

Nedergaard, J., and Cannon, B. (2014). The browning of white adipose tissue: some burning issues. Cell Metab. *20*, 396–407.

Nye, C.K., Hanson, R.W., and Kalhan, S.C. (2008). Glyceroneogenesis is the dominant pathway for triglyceride glycerol synthesis in vivo in the rat. J. Biol. Chem. *283*, 27565–27574.

Ohno, H., Shinoda, K., Spiegelman, B.M., and Kajimura, S. (2012). PPARγ agonists induce a white-to-brown fat conversion through stabilization of PRDM16 protein. Cell Metab. *15*, 395–404.

Pan, W.W., and Myers, M.G., Jr. (2018). Leptin and the maintenance of elevated body weight. Nat. Rev. Neurosci. *19*, 95–105.

Patterson, R.E., and Sears, D.D. (2017). Metabolic Effects of Intermittent Fasting. Annu. Rev. Nutr. *37*, 371–393.

Preitner, F., Muzzin, P., Revelli, J.P., Seydoux, J., Galitzky, J., Berlan, M., Lafontan, M., and Giacobino, J.P. (1998). Metabolic response to various beta-adrenoceptor agonists in beta3-adrenoceptor knockout mice: evidence for a new beta-adrenergic receptor in brown adipose tissue. Br. J. Pharmacol. *124*, 1684–1688.

Rababa'h, A., Singh, S., Suryavanshi, S.V., Altarabsheh, S.E., Deo, S.V., and McConnell, B.K. (2014). Compartmentalization role of A-kinase anchoring proteins (AKAPs) in mediating protein kinase A (PKA) signaling and cardiomyocyte hypertrophy. Int. J. Mol. Sci. *16*, 218–229.

Rebuffé-Scrive, M., Andersson, B., Olbe, L., and Björntorp, P. (1989). Metabolism of adipose tissue in intraabdominal depots of nonobese men and women. Metabolism *38*, 453–458.

Renehan, A.G., Tyson, M., Egger, M., Heller, R.F., and Zwahlen, M. (2008). Body-mass index and incidence of cancer: a systematic review and meta-analysis of prospective observational studies. Lancet *371*, 569–578.

Scheja, L., and Heeren, J. (2019). The endocrine function of adipose tissues in health and cardiometabolic disease. Nat. Rev. Endocrinol. *15*, 507–524.

Schreiber, S.N., Emter, R., Hock, M.B., Knutti, D., Cardenas, J., Podvinec, M., Oakeley, E.J., and Kralli, A. (2004). The estrogen-related receptor alpha (ERRalpha) functions in PPARgamma coactivator 1alpha (PGC-1alpha)-induced mitochondrial biogenesis. Proc. Natl. Acad. Sci. USA *101*, 6472–6477.

Seimon, R.V., Roekenes, J.A., Zibellini, J., Zhu, B., Gibson, A.A., Hills, A.P., Wood, R.E., King, N.A., Byrne, N.M., and Sainsbury, A. (2015). Do intermittent diets provide physiological benefits over continuous diets for weight loss? A systematic review of clinical trials. Mol. Cell. Endocrinol. *418*, 153–172.

Shin, H., Ma, Y., Chanturiya, T., Cao, Q., Wang, Y., Kadegowda, A.K.G., Jackson, R., Rumore, D., Xue, B., Shi, H., et al. (2017). Lipolysis in Brown Adipocytes Is Not Essential for Cold-Induced Thermogenesis in Mice. Cell Metab. *26*, 764–777.e5.

Stöckli, J., Zadoorian, A., Cooke, K.C., Deshpande, V., Yau, B., Herrmann, G., Kebede, M.A., Humphrey, S.J., and James, D.E. (2019). ABHD15 regulates adipose tissue lipolysis and hepatic lipid accumulation. Mol. Metab. *25*, 83–94.

Subramanian, A., Tamayo, P., Mootha, V.K., Mukherjee, S., Ebert, B.L., Gillette, M.A., Paulovich, A., Pomeroy, S.L., Golub, T.R., Lander, E.S., and Mesirov, J.P. (2005). Gene set enrichment analysis: a knowledge-based approach for interpreting genome-wide expression profiles. Proc. Natl. Acad. Sci. USA *102*, 15545–15550.

Sun, K., Tordjman, J., Clément, K., and Scherer, P.E. (2013). Fibrosis and adipose tissue dysfunction. Cell Metab. *18*, 470–477.

Sun, K., Park, J., Gupta, O.T., Holland, W.L., Auerbach, P., Zhang, N., Goncalves Marangoni, R., Nicoloro, S.M., Czech, M.P., Varga, J., et al. (2014). Endotrophin triggers adipose tissue fibrosis and metabolic dysfunction. Nat. Commun. *5*, 3485.

Sun, K., Park, J., Kim, M., and Scherer, P.E. (2017). Endotrophin, a multifaceted player in metabolic dysregulation and cancer progression, is a predictive biomarker for the response to PPARγ agonist treatment. Diabetologia *60*, 24–29.

Tol, M.J., Ottenhoff, R., van Eijk, M., Zelcer, N., Aten, J., Houten, S.M., Geerts, D., van Roomen, C., Bierlaagh, M.C., Scheij, S., et al. (2016). A PPARγ-Bnip3 Axis Couples Adipose Mitochondrial Fusion-Fission Balance to Systemic Insulin Sensitivity. Diabetes *65*, 2591–2605.

Tyanova, S., Temu, T., Sinitcyn, P., Carlson, A., Hein, M.Y., Geiger, T., Mann, M., and Cox, J. (2016). The Perseus computational platform for comprehensive analysis of (prote)omics data. Nat. Methods *13*, 731–740.

Varady, K.A., and Gabel, K. (2019). Safety and efficacy of alternate day fasting. Nat. Rev. Endocrinol. *15*, 686–687.

Varady, K.A., Allister, C.A., Roohk, D.J., and Hellerstein, M.K. (2010). Improvements in body fat distribution and circulating adiponectin by alternate-day fasting versus calorie restriction. J. Nutr. Biochem. *21*, 188–195.

Vitali, A., Murano, I., Zingaretti, M.C., Frontini, A., Ricquier, D., and Cinti, S. (2012). The adipose organ of obesity-prone C57BL/6J mice is composed of mixed white and brown adipocytes. J. Lipid Res. *53*, 619–629.

Wajchenberg, B.L. (2000). Subcutaneous and visceral adipose tissue: their relation to the metabolic syndrome. Endocr. Rev. *21*, 697–738.

Wang, M., Wang, Q., and Whim, M.D. (2016). Fasting induces a form of autonomic synaptic plasticity that prevents hypoglycemia. Proc. Natl. Acad. Sci. USA *113*, E3029–E3038.

Wilkinson, M.J., Manoogian, E.N.C., Zadourian, A., Lo, H., Fakhouri, S., Shoghi, A., Wang, X., Fleischer, J.G., Navlakha, S., Panda, S., and Taub, P.R. (2020). Ten-Hour Time-Restricted Eating Reduces Weight, Blood Pressure, and Atherogenic Lipids in Patients with Metabolic Syndrome. Cell Metab. *31*, 92–104.e5.

Xie, K., Neff, F., Markert, A., Rozman, J., Aguilar-Pimentel, J.A., Amarie, O.V., Becker, L., Brommage, R., Garrett, L., Henzel, K.S., et al. (2017). Every-other-day feeding extends lifespan but fails to delay many symptoms of aging in mice. Nat. Commun. *8*, 155.

Younossi, Z.M., Koenig, A.B., Abdelatif, D., Fazel, Y., Henry, L., and Wymer, M. (2016). Global epidemiology of nonalcoholic fatty liver disease-Meta-analytic assessment of prevalence, incidence, and outcomes. Hepatology *64*, 73–84.

Zechner, R., Madeo, F., and Kratky, D. (2017). Cytosolic lipolysis and lipophagy: two sides of the same coin. Nat. Rev. Mol. Cell Biol. *18*, 671–684.

STAR★METHODS

KEY RESOURCES TABLE

REAGENT or RESOURCE	SOURCE	IDENTIFIER
Antibodies		
HSL S660 antibody	Cell Signaling Technology	Cat #4126; RRID:AB_490997
ADRB3 antibody	Abcam	Cat #ab94506; RRID:AB_10863818
Chemicals, peptides, and recombinant proteins		
Acetonitrile	Thermo Fisher Scientific	Cat #FSBA955-4
Water	Thermo Fisher Scientific	Cat #FSBW6-4
Ethylacetate	Merck-Millipore	Cat #109623
Triscarboxyethylphosphine (TCEP) (Neutral pH solution)	Thermo Fisher Scientific	Cat #77720
Chloracetamide (CAA)	Sigma Aldrich	Cat #C0267
CL 316,243	Sigma Aldrich	Cat #C5976
10% neutral buffered formalin	Sigma Aldrich	Cat #HT501128
Critical commercial assays		
BCA total protein assay kit	Thermo Fisher Scientific	Cat #23225
CBQCA peptide & protein quantification kit	Thermo Fisher Scientific	Cat #C6667
Non-esterified fatty acid quantification kit	Wako	Cat #NEFAC-279-75401
Free glycerol determination kit	Sigma Aldrich	Cat #FG0100
Desposited data		
Data from this study.	ProteomeXchange Consortium PRIDE	PXD020255 and PXD023783
Experimental models: organisms/strains		
C57BL/6J Male Mice	Australian Bioresources	C57BL/6J
Software and algorithms		
R	R Project	Version 3.6.1
Tableau Desktop	Tableau	Version 2019.1.2
MaxQuant	https://www.maxquant.org/	Version 1.6.14

RESOURCE AVAILABILITY

Lead contact

Information and requests for reagents and resources should be directed to and will be fulfilled by the lead contact, Mark Larance (mark.larance@sydney.edu.au).

Materials availability

This study did not generate new unique reagents.

Data and code availability

The proteomic dataset generated during this study have been deposited to the ProteomeXchange Consortium (http://www.proteomexchange.org/) via the PRIDE partner repository with the dataset identifiers PRIDE: PXD020255 and PRIDE: PXD023783.

EXPERIMENTAL MODEL AND SUBJECT DETAILS

Mice

All experiments were carried out with the approval of the University of Sydney Animal Ethics Committee (2020/1893), following the National Health and Medical Research Council of Australia and ARRIVE guidelines. C57BL/6J male mice were obtained from Australian Bio-Resources (Moss Vale, Australia) and housed in groups of 5 in IVC cages on corn cob bedding (Bed-o'Cobs, Andersons, Maumee, USA). All mice were housed for at least one week prior to initiation of experimental models. Mice were housed in

temperature-controlled rooms (22°C) with a 12 h light/dark cycle (0600/1800 h) with *Ad libitum* food and water access (standard chow containing 12% calories derived from fat; 23% calories derived from protein and 65% calories derived from carbohydrates (Specialty Feeds, Australia).

Intermittent fasting model

Male mice at 8 weeks of age were randomly assigned into either *ad libitum,* or every-other-day-fasting (EODF) groups on a per cage basis. All cage bedding was changed to paper bedding (Pure-o'Cel, Andersons, Maumee, USA) for the duration of the model. Mice in the EODF group had total deprivation of food and *Ad libitum* access to water from 1200 h – 1200 h on alternate days with *Ad libitum* food and water access. EODF cages were changed upon induction of fasting. *Ad libitum* control mice cages were changed every other day with fresh food provided. At 1200 h every day, mice (individually) and food consumption (per cage) was weighed and recorded. Body composition was assessed at day 8 of study and blood glucose was measured at day 10 of study, with 2 cages (n = 10) allocated per treatment group. Study was terminated after 12 days with tissue collection initiated at 0850 h and concluded by 1050 h after an overnight period of feeding or fasting (1 cage, n = 5 per condition).

METHOD DETAILS

Determination of glucose tolerance

After an overnight period with *Ad libitum* food access, mice were fasted for 5 hours from 0800 h, before oral administration of 2g/kg glucose (25% v/v solution) per body weight by gavage and blood glucose monitored by Accu-Chek II glucometer (Roche Diagnostics) at regular time intervals by whole blood sampling from tail tip incision.

Body composition analysis

After an overnight period with *Ad libitum* food access, body mass (fat and lean mass) was measured at 0900 h using Magnetic Resonance Imaging (MRI) with an EchoMRI-900 Analyzer (EchoMRI, Houston, USA) in accordance with manufacturer's instructions.

Tissue collection

Between 0850 −1050 h, mice were sacrificed using CO_2 suffocation, and adipose tissue excised in the order: both epididymal fat pads, inguinal subcutaneous adipose then interscapular brown adipose tissue. All tissues were immediately snap frozen using LN_2 or used for lipolysis assessment.

Non-esterified fatty acid determination in plasma

Non-esterified free fatty acids (NEFAs) were measured in the plasma of mice according to manufacturer's instructions (Cat No. 279-7501, Waiko). Briefly, 2uL of plasma was diluted in sample diluent and background haemolysis determined by absorbance reading at 550nm. The solution was then incubated at 37°C for 10 mins and the second sample diluent added. Samples were incubated for another 10 mins at 37°C and then cooled at room temperature for 5 mins. The absorbance was subsequently measured at 550nm for standard curve generation and NEFA concentration determination.

Lipolysis assay

Lipolysis assays were performed as previously described (Stöckli et al., 2019) with minor modifications. Mouse visceral epididymal fat explants were incubated with indicated concentrations of CL316,243 (Cat No. C5976, Sigma Aldrich) for 1 h and glycerol release into the media was measured using the free glycerol determination kit (Cat No. FG0100, Sigma Aldrich). Fat explants were lysed in 100 mM NaOH for protein determination and assay normalization.

Histopathology

All tissues were fixed in 10% neutral buffered formalin for 48 h at RT, washed with 70% ethanol and stored at 4°C in 70% ethanol. Tissues were dehydrated and embedded in paraffin before sectioning. Individual sections were stained with either hematoxylin & eosin (H&E), or picrosirius red. Digital images of each slide were collected using a Zeiss upright Axioscope A1 (Zeiss) microscope between 5-20 x magnification. Images shown are representative results from 10 biological replicates per condition.

Sample preparation of adipose tissue for protein mass-spectrometry

Frozen adipose tissue was lysed in 4% sodium deoxycholate (SDC), 100mM tris-HCl (pH 8.5) and 10mM N-ethylmaleimide (NEM) at RT using an Ultra-Turrax T8 stick homogensier (IKA ® - Werke) to blend the tissue prior to immediate heating of the lysates to 95°C for at least 10 min. Then, lysates were sonicated at 70% amplitude for 15:15 s pulses for 10 min on-time at RT using a Q800R2 sonicator (QSonica, Connecticut, USA). Lysates were clarified by chloroform-methanol precipitation (see Chloroform-methanol precipitation).

Chloroform-methanol precipitation

Protein lysates post-sonication were clarified by chloroform/methanol precipitation. Where, 1-part (200uL) lysate was mixed with 4-parts (800uL) methanol and vortexed for 1 min. Next, 2-part (400ul) chloroform was added and vortexed for 1 min. Lastly, 3-parts (600ul) MQ water were added and vortexed until solution was completely milk-white. Solution was centrifuged at 7,000 *x g* for 5 min, if solution was still cloudy, centrifugation was repeated. The top aqueous phase was aspirated until 1cm above the protein suspension and 3-parts (600ul) methanol was added and the solution vortexed for 1 min. Centrifugation was repeated at 7,000 *x g* for 5 min, if solution was still cloudy, repeat centrifugation until clear. All liquid was carefully aspirated, and protein pellet air-dried in a recycling fume hood for 5 min. Pellet was resuspended in 4% SDC and 100mM Tris-HCl (pH 8.5) prior to heating to 95°C for at least 30 min or until most of the pellet was resuspended. Lysate was then clarified by centrifugation at 18,000 *x g* for 10 min and supernatant taken for subsequent steps.

Trypsin digestion for proteome analysis

Protein concentration was determined by BCA total protein assay (Pierce) or CBQCA total protein assay (ThermoFisher). 20ug of protein was reduced with 10mM TCEP and alkylated with 40mM chloroacetamide simultaneously at 95°C for 1 h. Lysates were then diluted to a final concentration of 1% SDC using MQ water and digested overnight with 400ng MS-grade trypsin (in 50mM acetic acid) at 37°C with constant rocking. Samples were diluted with ethyl acetate (50% final concentration, v/v) and vortexed until all the precipitated SDC was resuspended. StageTips were prepared and sample purification performed as done previously (Harney et al., 2019a), with the addendum that only the top aqueous phase of the sample was added to the StageTips. Peptides were reconstituted with 5% formic acid in MS-grade water, sealed and stored at 4°C until LC-MS/MS acquisition.

High pH reverse-phase LC fractionation

Peptides sample prepared as in Trypsin digestion for proteome analysis, were pooled with 1ug taken from each sample. 10ug of peptide sample in 5% formic acid was injected onto a Waters acuity UPLC Peptide BEH C18 column (130A, 1.7um, 2.1mm x 150mm) on a Thermofisher Dionex UltiMate 3000 LC in 5% acetonitrile and 10mM ammonium formate (pH 9.2). Peptides were resolved over 30 min on a 5%–80% acetonitrile gradient with the samples collected from 2-16 min into a low-protein binding plate (ThermoFisher) in a 16-well concatenated fashion. Fractions were dried, resuspended in 50% acetonitrile and 0.1% trifluoracetic acid in LC-grade water, transferred into low-profile PCR plate, dried again and resuspended in 5% formic acid. Samples were sealed and stored at 4°C until LC-MS/MS acquisition.

Protein LC-MS/MS and spectra analysis

Peptide samples prepared as in Trypsin digestion for proteome analysis, were directly injected onto a 30cm x 70 um C18 (Dr. Maisch, Ammerbuch, Germany, 1.9 um) fused silica analytical column with a 10 μm pulled tip, coupled online to a nanospray ESI source. Peptides were resolved over a gradient from 5% - 40% acetonitrile over 120 min with a flow rate of 300 nL min^{-1}. Peptides were ionized by electrospray ionization at 2.3 kV. MS/MS analysis was performed using either a Q-Exactive HFX or Q-Exactive Fusion Lumos mass spectrometer (ThermoFisher) with HCD fragmentation. Spectra were attained in a data-dependent acquisition of the top 20 most abundant ions at any individual point during the gradient. RAW data files including the high pH fractions were analyzed using the integrated quantitative proteomics software and search engine MaxQuant (Cox et al., 2014) (version 1.6.14), and the MaxQuant output has been uploaded to ProteomeXchange Consortium under the identifier PXD020255 (Username: reviewer90496@ebi.ac.uk, Password: dLhwS7HH) (http://proteomecentral.proteomexhange.org). A false discovery rate of 1% using a target-decoy based strategy was used for protein and peptide identification with protein filtering such that all proteins must have > 2 razor and unique peptides. The database provided to the search engine for identification contained the Uniprot mouse database downloaded on the 5th of May 2020 alongside the MaxQuant contaminants database. Mass tolerance was set to 4.5 ppm for precursor ions and MS-2 mass tolerance was set to 20 ppm. Trypsin was set as the digestion enzyme with a maximum of 2 missed cleavages. Deamidation of Asn and Gln, pyro-Glu, carbamidomethylation of Cys, N-ethylmaleimide modification of Cys and protein N-terminal acetylation were set as variable modifications. There were no fixed modifications. The MaxLFQ algorithm was used for label-free quantitation, integrated into the MaxQuant environment (Cox and Mann, 2008; Cox et al., 2011). Data was processed as in Quantification and statistical analysis.

Targeted mass spectrometry of beta-adrenergic receptors

Peptides were resolved over a gradient from 5%–40% acetonitrile over 35 min with a flow rate of 300 nL min^{-1}. Peptides were ionized by electrospray ionization at 2.3kV. MS/MS analysis was performed using a Q-Exactive Fusion Lumos mass spectrometer with HCD fragmentation. All spectra were acquired at 60,000 resolution in profile mode with a maximum injection time for MS/MS of 118 ms using an isolation width of 0.7 m/z and normalized HCD collision energy of 30% with parallel reaction monitoring (PRM). MS/MS spectra were acquired for tryptic peptides derived from ADRB1 (YQSLLTR, m/z = 440.74798, z = 2) and ADRB3 (AVTFPASPVEAR, m/z = 622.83532, z = 2). Background interference was determined by comparison to blank runs. Spectra were quantified using Xcalibur Qual Browser (ThermoFisher), where peak area of the most abundant transition was measured with a 5-ppm error window. For each peptide the transition measured was: ADRB1; y_6 ion of YQSLLTR (m/z = 717.4254) and ADRB3; y_8 ion of AVTFPASPVEAR (m/z = 826.4417). Peak area was normalized to peptide concentration as determined by CBQCA assay which was performed as described previously (Harney et al., 2019a).

QUANTIFICATION AND STATISTICAL ANALYSIS

The animal number required for each treatment group was established based for prior intermittent fasting studies (Hatchwell et al., 2020). All proteomics data was analyzed using R (version 3.6.1) and plotted using Tableau (version 2019.1.2), outliers greater than 1.5 times the inter-quartile range were excluded for some plots to aid visualization. Fold changes were calculated based on median values on a per group basis. Imputation was used for statistical analysis where the mean and standard deviation was determined for each protein using the three lowest values which was used to impute values for proteins. A protein was imputed if the protein was detected in 1 or 2 out of 5 samples in a condition and detected in > 3 samples in every other condition (Tyanova et al., 2016). Statistical significance was determined using a two-way ANOVA for diet (*Ad libitum* versus EODF), harvest state (fed versus fasted) and interaction between the two conditions. Outputs were corrected for multiple testing using the Benjamini-Hochberg correction, with significance being set at $p < 0.05$ at an FDR of 5%. High pH RP fractions were not included in fold change or statistical analysis.